

FABRICATION AND CHARACTERIZATION OF SPIN HALL NANOWIRE
WITH CONSTRICTED GEOMETRY

A Thesis

Presented to the Faculty of the Graduate School

of Cornell University

In Partial Fulfillment of the Requirements for the Degree of

Master of Science

by

Albert Min Gyu Park

August 2016

© 2016 Albert Park

ABSTRACT

Spin torque oscillators, which use spin dynamics in ferromagnetic materials to generate rf frequencies, are a promising candidate for on-chip rf oscillators due to their nanoscale size, broad frequency range, and fast response time. However, drawbacks such as small power output and broad linewidth have been obstacles for commercial applications of spin torque oscillators. In this thesis, we study an approach aimed at combining mutual phase locking with recently developed spin Hall nano-oscillators intended to overcome the current challenges. In the first part of this thesis we will review the background of spin-torque oscillators and establish a fabrication process for spin Hall nanowires with constrictions that will be used to test our ideas. Spin torque ferromagnetic resonance measurements and electrical measurements of the spectral power output will be used to characterize the properties of spin Hall nano-constricted devices, as well as to analyze their magnetic modes. Finally, we will discuss future directions for mutual phase locking with spin Hall nano-constricted devices.

BIOGRAPHICAL SKETCH

Albert Park was born on February 28, 1990 in Palo Alto, CA. He attended the Korea Advanced Institute of Science and Technology (KAIST) and earned a dual Bachelor of Science degree in Physics and Electrical Engineering. He also earned a Master of Science degree in Electrical Engineering at the same institute. He enrolled at Cornell University in the School of Applied Engineering and Physics, where he studies on nanospintronics in the Fuchs research group.

ACKNOWLEDGMENTS

I would like to begin by thanking my advisor Gregory David Fuchs for guiding and helping me throughout the whole project. This work wouldn't have been possible without his deep insight and experience in the field, as well as his enthusiasm and supportiveness. It was truly an honor to work with him.

I would like to thank David Muller for his guidance as director of the Master of Science program, for being on my committee and for providing helpful advice for my studies.

I would also like to thank all of the great colleagues I met in the group. Emrah Turgut and Feng Guo, helped me a lot on getting used to the experimental setup and concepts of magnetic measurements. Darryl Ngai and Jack Mingde Jiang provided me with lots of useful information about fabrication process of magnetic devices. Austin Moehle taught me much about how to operate a magnetic setup that was used in this work. All of the members of our group, Evan McQuarrie, Nick Jungwirth, Jason Bartell, Isaiah Gray and Jonathan Karsch, were never reluctant to answer questions I had or help me with problems that I faced during the project.

I would also like to thank Steven Kriske who trained me on a lot of the CCMR facilities at Clark Hall including TPT wire bonder, 3-gun sputtering system, and the 4-point probe. I thank Alan Bleier and Amrita Banerjee for helping me with e-beam lithography and scanning electron microscopy. I thank Garry Bordonaro, Jerry Drumheller, Daniel McCollister and Sam Wright who helped me with photolithography processing, the profilometer, the AJA ion mill and the Disco dicing saw, and all the CNF staff who helped me out in cleanroom. I thank Cynthia Reynolds, Renee King and Donna Mazza for their kindness and support with administrative issues.

Outside of our group, I would like to thank all of my Master of Science colleagues including Steven Kiekel, Maxwell Fishman, Alejandro Carderera, Reet Chaudhuri, Yunsheng Wang, Mingtong Han, Di Ni and Qiannan Wen who helped me a lot in getting used to and making the life enjoyable in Ithaca.

TABLE OF CONTENTS

Biographical Sketch	iii
Acknowledgement	iv
Table of Contents	vi
List of Figures	vii
1. Introduction	
1.1 General Overview	1
1.2 Spin Hall Effect	1
1.3 Spin Transfer Torque, LLGS and Spin dynamics in Ferromagnet	5
1.4 Spin Torque Oscillators	9
2. Fabrication of Spin Hall Nanowires with Constricted Geometry	
2.1 Device Design	17
2.2 Fabrication Methods	19
3. Characterization Methods	
3.1 Spin Torque Ferromagnetic Resonance	23
3.2 Heterodyne Spectrum Analyzer	26
3.3 Calculation of Power Spectrum Density	29
4. Results and Analysis	
4.1 STFMR Results	34
4.2 STFMR Analysis	36
4.3 Auto-Oscillation Properties	38
4.4 Relation between auto-oscillation and STFMR for constricted samples	41
5. Concluding Remarks	44
Bibliography	46

LIST OF FIGURE

1-1.	Schematic description of spin Hall effect.....	3
1-2.	Three different mechanisms of spin Hall effect	4
1-3.	Illustration of the magnetization precession and directions of damping and spin-torque vectors	9
1-4.	Various types of geometries for various geometries of STNO and SHNO.....	11
1-5.	Experiment with spin current through the extended magnetic film	12
1-6.	Spin torque oscillator using spin Hall nanowire.....	13
1-7.	Device geometry and emission spectra for phase locked nanocontact STOs .	16
2-1.	Device designs.....	18
2-2.	Design of flare-out.....	18
2-3.	Fabrication process flow diagram	20
2-4.	SEM image of fabricated devices.....	21
3-1.	STFMR Schematics.....	25
3-2.	Microwave circuitry for the STFMR measurement	26
3-3.	Schematics of microwave circuitry for home-built spectrum analyzer	27
3-4.	Circuit diagram of the sample and the microwave circuit	27
3-5.	Photograph of the experimental setup for the heterodyne spectrum analyzer .	29
3-6.	Difference in lock-in voltage for 50 Ohm termination at room temperature and in the liquid nitrogen temperature	31
3-7.	Corrected difference in lock-in voltage for 50 Ohm termination at room temperature and in the liquid nitrogen temperature	31
3-8.	Conversion rate for PSD-to-lock-in-voltage ratio	32
3-9.	Raw data for the auto-oscillation and the integrated data	33
4-1.	STFMR signal for a device with two constrictions	34

4-2.	Full trend of spectrum of STFMR for device 1	35
4-3.	Full trend of spectrum of STFMR for device 3	36
4-4.	Comparison of STFMR for magnetic field applied at different angles	37
4-5.	Current dependence of STFMR resonance signal for magnetic field applied at 45°	38
4-6.	Current dependence of an auto-oscillation signal	39
4-7.	Magnetic field dependence of an auto-oscillation	40
4-8.	Plot of resonance peaks measured using STFMR and auto-oscillation	42
4-9.	Rf current and dc current configurations for analyzing the current dependence of STFMR	43

CHAPTER 1

INTRODUCTION

1.1 General Overview

The field of spintronics refers to the area of study for which both the spin and the charge properties of an electron are considered for new scientific discovery and engineering applications. This area of study, which combines magnetism and electrical engineering, blossomed for more than decades. Magnetic storage devices, which are still being used for the main or auxiliary storage of virtually all the computers in the world, are one of the great developments that can be considered as spintronic devices. Along with technology that is prevalently found in everyday appliances, spintronics is promising for the development of spin-transfer torque magnetic random access memory and spin-transfer torque radio frequency oscillators

Among recent developments are electronic and magnetic devices that incorporate the spin Hall effect. Although many spin Hall devices have been proposed including switching devices [1,2], transistors [3,4], and oscillators [5–10], we focus on devices that use the spin Hall effect and spin transfer torques for manipulation of a magnetic system. More specifically, recently developed spin Hall oscillators with nano-size geometries will be discussed. In this chapter we present an overview of a spin Hall devices and the relevant physical background.

1.2 Spin Hall Effect

Brief History and Introduction

The spin Hall effect was first theoretically predicted in 1971 by Dyakonov and Perel [11,12]. In these seminal papers, the authors predicted that a charge current, in

the presence of spin-orbit coupling, can create a net spin accumulation at the boundary of the sample. This can be understood as an effect similar to a Mott scattering, which occurs for an electron beam that scatters off heavy ions. In the case of Mott scattering, the spin-orbit term in the scattering potential causes a scattering cross section difference between up and down spin electrons. As will be discussed in following subsection, the solid state nature of the spin Hall effect brings about more complex behavior than the simple Mott-like picture.

As its name indicates, the spin Hall effect is named in analogy to the normal Hall effect, in which charge is accumulated at the sample edge due to a charge current in a magnetic field. Moreover it originates from nearly the same principle as the anomalous Hall effect, where additional accumulation of charge is observed depending on the magnetization of the material. The main phenomenological difference between the normal Hall effect and the spin Hall effect comes from the fact that the quantity being accumulated is spin rather than charge. Note that spin is not a conserved quantity. Thus, concepts such as decay length and dephasing become important for quantitative descriptions of the spin Hall effect. Also, unlike its cousin effects, the spin Hall effect requires no magnetic field for the accumulation of the spin.

Although there is a rich literature of theoretical works on this topic, in this subsection we will briefly discuss about the mechanism of the spin Hall effect and the transport experiments using magnetic multilayer stack which are relevant to main topic of the thesis.

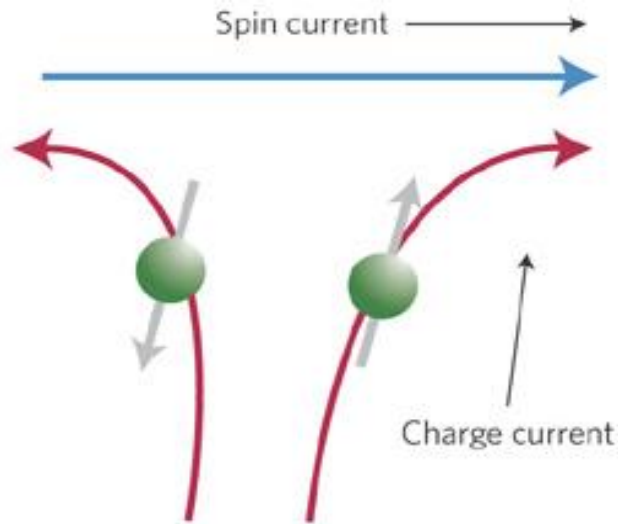


Fig 1-1. Schematic description of spin Hall effect [13]

Theory – Mechanism and Phenomenology

The mechanism of the spin Hall effect can be categorized as either extrinsic or intrinsic. In the extrinsic mechanism, impurities play an important role and this again can be divided into two mechanisms: skew scattering and side jumping. [14]

Skew-scattering can be understood from a semi-classical treatment of Boltzmann transport theory. In presence of spin-orbit coupling, the existence of an asymmetric chiral contribution results in a different probability between right-handed and left-handed transitions with respect to the direction of magnetization.

The side jump mechanism also arises from spin-orbit coupling, but while skew-scattering comes from a chiral contribution, the side-jump mechanism originates from the scattering of a Gaussian wave packet in presence of a spherical impurity. Because dimensional confinement is important for skew scattering, it is the dominant mechanism in 2D materials and semiconductor 2 dimensional electron gas. On the other hand, it has been suggested that the side jumping mechanism can have an effect in metals including Pt [15].

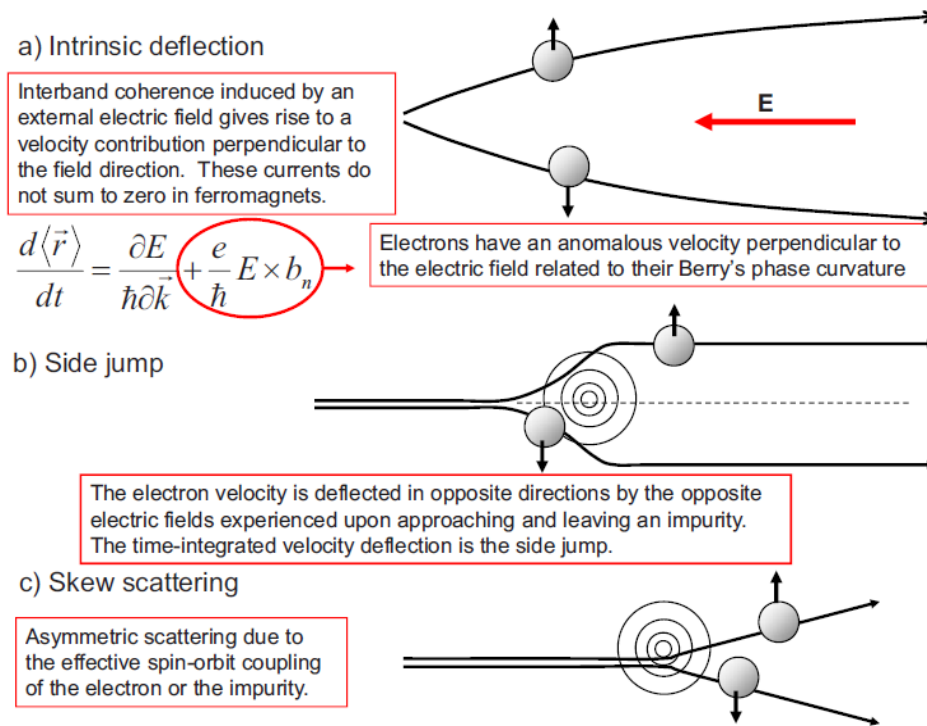


Fig 1-2. Schematic description of three different mechanisms of the spin Hall effect [16]

While the impurity and the scattering potential are important for side jump and skew scattering, the intrinsic effect arises from the band structure of solid crystal. Under an electric field, accelerated electrons feel an induced, momentum-dependent magnetic field. This leads to the separation of electrons with different spin projection, and hence the spin accumulation. Schematic description of each mechanism can be seen from Fig 1-2.

Transport Experiments

The spin Hall effect was experimentally confirmed in metallic, semiconductor and insulating systems by various methods. Although the first experimental confirmation of the spin Hall effect was made using optical detection [17,18], it was already

predicted by the earliest theoretical works that transport measurements will be an intuitive method to detect spin Hall effect [19,20].

The first experimental works that verified the sign of the spin Hall effect using transport used a nonlocal device. While a current passing through the spin Hall metal creates a spin-polarized current, the inverse process (generating a voltage from a spin-polarized current) known as the inverse spin Hall effect, is also possible. Valenzuela and Tinkham [21,22] used a device that had a ferromagnetic electrode to inject spin polarized current into a normal metal (Al). Saitoh *et al.* [23] independently obtained a similar result using a spin-pumping effect to inject spin from a ferromagnetic layer into normal layer. In 2007, using similar device, Kimura *et al.* [24] succeeded in obtaining both the inverse and the normal spin Hall effect.

More recently, a method of measuring the spin Hall effect using ferromagnetic resonance of an adjacent ferromagnetic layer was proposed and verified [1,25]. How this works will be further described in section 3-1.

1.3 Spin Transfer Torque , LLGS, and Spin dynamics in Ferromagnet

Spin-transfer torque can be understood as an angular momentum transfer. When current with non-zero spin polarization is injected into a ferromagnetic layer, it exerts torque on a magnetization.

To understand this quantitatively, we develop the basic formalism of magnetization dynamics and then add an additional term that describes the influence of spin-transfer torque. The starting point is Larmor precession, which describes a motion of magnetization in presence of magnetic field according to

$$\frac{d\mathbf{M}}{dt} = -\gamma_0 \mathbf{M} \times \mathbf{H}_{\text{eff}} , \quad (1.1)$$

where γ_0 is a gyromagnetic ratio, \mathbf{M} is magnetization and \mathbf{H}_{eff} is effective magnetic field. Equation (1.1) shows that in presence of effective magnetic field \mathbf{H}_{eff} , magnetization precess around the direction of magnetic field. The components that contribute to the magnetic energy density can be represented as a field by taking the functional derivative of energy density with respect to magnetization. \mathbf{H}_{eff} is the vector sum of all such fields that act on the magnetization including the magnetocrystalline anisotropy, the demagnetization field, the exchange interaction and the external field.

Equation (1.1) does not fully describe the dynamics of magnetization because it does not account for energy loss. The way to account for loss of energy was devised by Landau and Lifshitz. This was done by adding an additional term that has the form of a torque on a magnetization but in a direction such that the system will lose energy and align with direction of effective magnetic field.

$$\frac{d\mathbf{M}}{dt} = -\gamma_0 \mathbf{M} \times \mathbf{H}_{\text{eff}} - \frac{\lambda}{M_s} \mathbf{M} \times (\mathbf{M} \times \mathbf{H}_{\text{eff}}) \quad (1.2)$$

The new term is known as the damping term and is multiplied by coefficient λ/M_s . λ is a phenomenological constant that describes the rate of the damping and M_s is a saturation magnetization which is included to preserve the total magnitude of magnetization.

The damping term was later modified by Gilbert as a representation which can be described as a viscous torque [26]. Thus the Landau-Lifshitz-Gilbert (LLG) equation we present as equation (1.3) is commonly used now.

$$\frac{d\mathbf{M}}{dt} = -\gamma \mathbf{M} \times \mathbf{H}_{\text{eff}} - \frac{\alpha}{M_s} \mathbf{M} \times \frac{d\mathbf{M}}{dt} \quad (1.3)$$

Since the damping term has a time derivative of magnetization (a vector) in generalized coordinates, each component can be considered separately. The Landau-Lifshitz form (1.2) is mathematically identical to (1.3) and can be deduced from (1.3) by multiplying \mathbf{M} on each side and using the vector identity. The relationship between coefficients in each form is given by $\gamma = \gamma_0(1 + \alpha^2)$ and $\lambda = \gamma\alpha / (1 + \alpha^2)$. α is the unitless Gilbert damping constant, which depends on material and thickness, but is usually in range of 0.1 to 0.001 for a ferromagnetic material.

The LLG equation is still considered the best way to describe the dynamics of magnetization phenomenologically, however in 1996 an important theory was derived that predicted an additional torque term when a spin-polarized current is injected into a ferromagnetic layer [27,28]. This modifies the LLG equation with a spin transfer torque (STT) term as described by Slonczewski and Berger as

$$\frac{d\mathbf{M}}{dt} = -\gamma\mathbf{M} \times \mathbf{H}_{\text{eff}} - \frac{\alpha}{M_s} \mathbf{M} \times \frac{d\mathbf{M}}{dt} + \gamma \frac{j_c \hbar \varepsilon}{2edM_s^2} \mathbf{M} \times (\mathbf{M} \times \mathbf{m}_f), \quad (1.4)$$

where j_c , ε , e , \hbar and d represent charge current density, injection efficiency, electron charge, the reduced Planck constant and thickness of the ferromagnetic layer, relatively. For typical magnetic devices, the charge current density for which this term dominates the dynamics is in range of 10^7 to 10^9 A/cm². Also, the thickness of the ferromagnetic layer is typically a few to tens of nanometers, depending on the purpose. The injection efficiency ε is a unitless phenomenological constant that accounts for details including spin polarization, interface properties and spin decoherence, and which typically has a value of less than 1 for most spin valve and tunneling devices. In case of spin valves, \mathbf{m}_f is a magnetization direction of a fixed layer but it can be

generalized as a spin torque unit vector which represents the direction of spin-polarization of the electrons for spin current injected on ferromagnetic layer.

When the spin Hall effect is used to inject spin-polarized current, we can use almost an identical equation with a slightly modified spin-torque term. First, to address the conversion factors for spin current and charge current, we can use an additional fractional term α_{SH} , which is often called spin hall angle. Also, to address the direction of spin polarization, we will use $\boldsymbol{\sigma}$. Thus we can write spin current density as $\mathbf{j}_s = \alpha_{SH} j_c \boldsymbol{\sigma}$. Using this as our new spin current density the last term from (1.4) can be modified as below [14].

$$T_{STT} = \gamma \alpha_{SH} \frac{j_c \hbar \varepsilon}{2edM_s^2} \mathbf{M} \times (\mathbf{M} \times \boldsymbol{\sigma}) \quad (1.5)$$

Again, similar to the injection efficiency, α_{SH} hides many of details in the form of a phenomenological and unitless coefficient. However, it can be directly obtained from experiments. It should be noted that the value can vary widely depending on the experimental geometry that is being employed. For instance, using the non-local geometry, the spin Hall angle of Pt (a material known to have among the highest spin-orbit coupling), is measured to be less than a percent [24,29]. If, however, spin pumping or injection into a ferromagnet is used to measure the spin Hall angle, the percentage increases to nearly a ten percent [25,30].

1-4. Spin Torque Oscillators

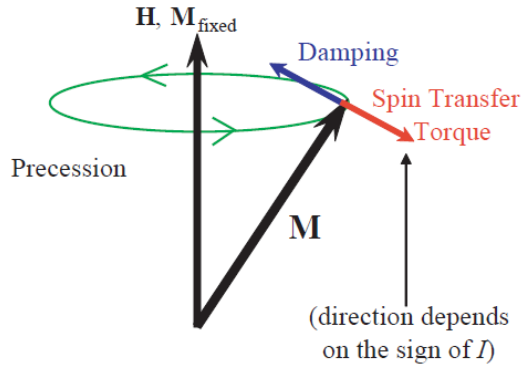


Fig 1-3. Illustration of the magnetization precession and directions of damping and spin-torque vectors [31]

As can be seen from Fig 1-3, when the current induced anti-damping torque and the viscous damping of the ferromagnetic layer have a same magnitude, the steady-state is for the magnetization to oscillate in a stable, precessional orbit. As it precesses, the intrinsic resistance of the ferromagnet changes due to the anisotropic magnetoresistance, which results in the electric ac signal. This means that ac power of a certain frequency can be generated by a dc current. Such devices are called spin torque oscillators (STO).

Types of spin torque oscillator

STOs using giant magnetoresistance (GMR) or tunnel magnetoresistance (TMR) stacks generate a spin polarized current with a fixed ferromagnetic layer, and have been studied for long time. A first challenge faced by the pioneers of STOs was the high current density required to generate enough anti-damping torque. For the first experimental demonstration of magnetization precession under STT [32], this problem was solved by creating a small mechanical point contact with area on the order of 100 nm^2 . With such a small contact area, the authors were able to obtain a current density

of 10^9 A/cm² using a total current in the milliamp range. Using nanofabrication technology including electron beam lithography and ion mill etching, more advanced geometries such as nanopillar or nanocontact devices were proposed and tested. (Fig 1-4. (a) -(d))

For the nanopillar geometry, the current flows through the entire multilayer stack which reduces the operating current density to near 10^7 A/cm², an order of magnitude lower than what is required for other geometries. As a tradeoff, the small volume of the dynamic magnetic layer is more vulnerable to phase noise. This eventually increases the linewidth and the device-to-device variation. Nanocontact devices, on the other hand, have an extended stack that is connected to an elliptical or circular electric contact area on the order of 100 nm². Physically, this is similar to its mechanical contact predecessor, but it can have a better oscillation signal and mechanical robustness because i) the contact was chemically formed reducing the interfacial defects and ii) the insulator provides better insulation than air. Compared to the nanopillar structure, nanocontacts have better linewidth and device uniformity, however, shunting current through the extended layer results in a typically higher current density of 10^8 - 10^9 A/cm². Hybrid “sombbrero”-shaped geometry were also proposed to corroborate the strong points of two geometries [33,34].

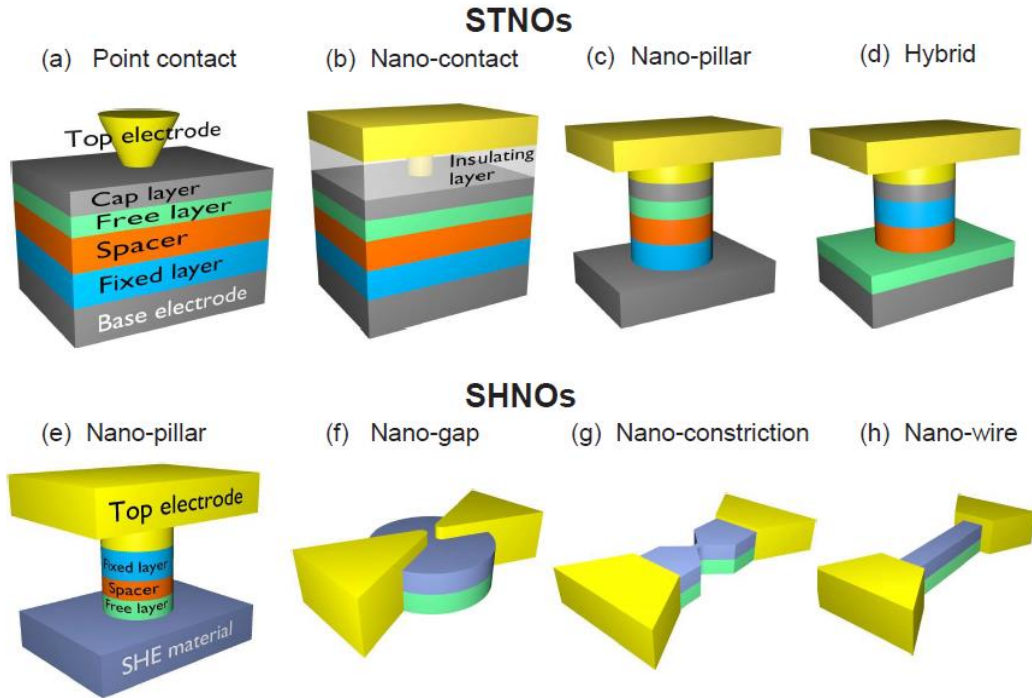


Fig 1-4. Various types of geometries for spin torque nano oscillators (STNO) and spin Hall nano oscillators (SHNO) [35]

More recently it has been shown that the spin Hall materials can generate a spin current, and used in a similar way as a magnetic fixed layer to generate an oscillatory motion of magnetization [5–10]. While there is a hybrid approach that uses a magnetic tunnel junction (MTJ) element as a more efficient electrical read-out method for the oscillation of the free layer, [2,8], simpler ferromagnet/Pt bilayers also exhibit the oscillation properties.

Similar to GMR or TMR based nano-oscillators, spin Hall oscillators also require a confinement of current. To achieve this, nanocontact and other constricted geometries have been used.

We have explained above that large spin current density is required to start a magnetic oscillation, and that this was achieved by reducing the area of current flow. However, what would happen if we pass a strong enough current density through an

extended layer, such that the required spin current is present throughout the whole layer? Would it induce a synchronized motion of magnetization? Of course this would also bring about excessive joule heating, so it would be hard to test out in GMR or TMR devices, but for spin Hall structures, the separation of charge current and spin current makes possible to get a large enough, uniform current throughout an extended structure. Experimental studies have shown that uniform and large enough spin current through an extended geometry does not excite a uniform mode auto-oscillation [31]. As it can be observed from Fig 1-5, the broad Lorentzian curve measured from the Brillouin light scattering (BLS) revealed that for extended film all spin-wave modes are excited by a spin current and cause a strong nonlinear interactions. This is clear from Fig 1-6. (c), where we can see the presence of energy and momentum conserving four magnon scattering for spectrum of spin wave propagating parallel to the in-plane magnetization vector. The scattering channel cause the damping of the uniform mode ($\mathbf{k}=0$) into wave modes with finite wave vector \mathbf{k}_4 .

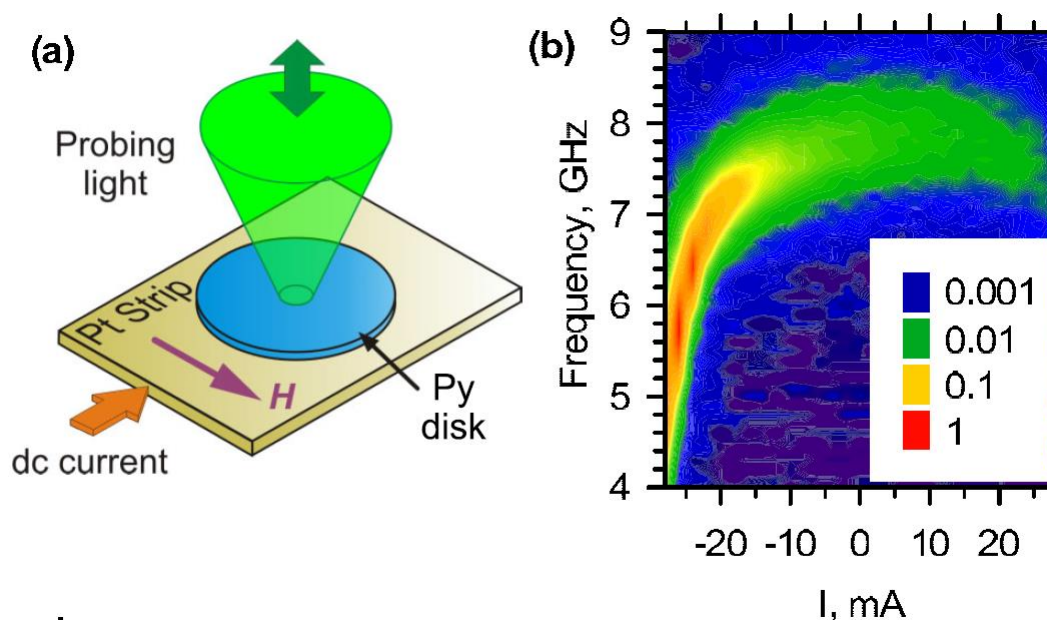


Fig 1-5. (a) Schematic of the experiment with spin current through the extended magnetic film and (b) the Brillouin light scattering intensity from the experiment which shows increased magnetic fluctuation but no uniform mode oscillation [31].

While the result from Demidov *et al.* [31] showed the impossibility of auto-oscillations in extended films, and other works confined a spin current into a small point-like region to generate a local magnetization oscillation, the work by Duan *et al.* [5] revealed that auto-oscillations and ferromagnetic resonance can be observed when the width of a ferromagnetic nanowire is narrower than a critical value. This was rather surprising because it showed that by confining to only a single spatial dimension, nonlinear magnon scattering processes that apply to all spin-wave modes can be suppressed to enable auto-oscillation. Again from Fig 1-6.(c) when a film is patterned to have width narrower than πk_4^{-1} , energy and momentum conserving four magnon scattering is suppressed because the spectrum of spin wave propagating parallel to the in-plane magnetization vector are quantized. Therefore, nonlinear spin-wave scattering become energy nonconserving.

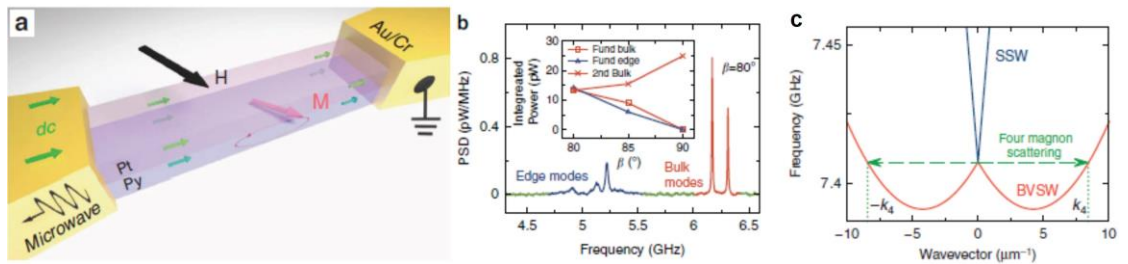


Fig 1-6. (a) Schematic of a sample structure and (b) microwave emission spectra for STO using spin Hall nanowire with Pt and Py stack. (c) Spin wave dispersion curve of 5 nm thick Py film [5].

Advantage and challenges of spin torque oscillator

As we discussed previously, to create a high enough current density, the devices need to be small. This in turn is an advantage for integration with applications for mobility and increased performance. While commonly used microwave oscillators such as voltage-controlled oscillators, or dielectric resonator oscillators require

footprints of area mm^2 to cm^2 , STOs are nano-sized by nature. This makes an STO an attractive candidate for an on-chip microwave oscillators.

Next we discuss how the frequency of magnetic precession depends on magnetic field. The uniform precessional mode evolves with field as described by the Kittel formula

$$\omega = \gamma \sqrt{H_{DC} (H_{DC} + 2\pi M_s)}, \quad (1.6)$$

where H_{DC} is the applied magnetic field and M_s is the saturation magnetization. We have assumed a magnetic layer in the thin film limit with negligible anisotropy field. As it can be seen from (1.6), the oscillation frequency increases with the applied magnetic field, enabling field tunability over a wide range. Typical oscillation frequencies range from 1-10GHz, but low frequency of 100 MHz and high frequency of up to 50 GHz has been reached for different geometries of STO.

Also, since the spin relaxation time is short, the auto-oscillation can adjust to a changed condition in order of nanoseconds. This agility of STOs make them attractive for modulation and demodulation of rf signals, which is a key capability for modern communication devices.

On the other hand, so far STOs have not managed to take part in commercial devices. Major problems that STOs face is that they produce low output power, a linewidth that is not narrow enough for applications, and they lack robustness. So far the highest power reported from a STO is in range of a microwatt [37], and most STOs have nW to pW output powers. Because power output in the mW range is desirable for applications, a STO needs some power boost to be considered as a viable candidate for technology. The broad linewidth of the STO can come from different mechanisms depending on the geometry. For instance, nanopillars have broadened linewidths at

room temperature due to mode-hopping [38–40]. Also, because STOs are small, they are prone to phase noise coming from Brownian motion and this often causes a linewidth that varies with temperature and applied current [41,42]. Such nonlinear effects are not desired for applications.

Finally, because high current is required for STOs, their lifetime is not very long. Also edge effects and nonlinear effects such as mode hopping can reduce the reliability of the device. Such issues need to be solved before we enjoy the advantages of STOs discussed formerly.

Mutual Phase Locking of Spin Torque Oscillators

One way that has been suggested to overcome the shortcomings of STOs is by locking the phase of multiple oscillators. In particular, it is known to increase power output and decrease linewidth [43–46]. So far, mutual phase locking has been demonstrated in STO with nanocontact geometry [44–46]. As shown in figure 1-7, as current through the oscillators are controlled, two nanocontact oscillators can oscillate with the same phase and frequency. The result amounts up to larger power and the narrower bandwidth as figure 1-7 (c) and 1-7 (e) shows.

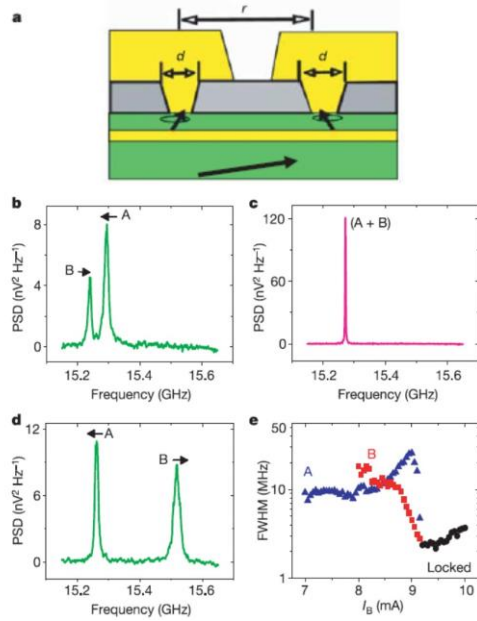


Fig 1-7. (a) Device geometry for two phase locked nanocontact STOs. Microwave emission spectra when the current is (b) lower than, (c) the same as, and (d) higher than required for the mutual phase locking. (e) Linewidth properties of two STOs before and after the locking [45].

Mutual phase locking is possible due to coupling mediated by propagating spin waves [47,48]. This brings up a possibility that mutual phase-locking can also be realized in spin Hall nano oscillators that have recently been developed.

This idea led us to think about creating multiple constricted regions over a spin Hall nanowire that would enable mutual phase locking of the auto-oscillations at each constriction site. Also, we intend to study how to optimize the parameters for the engineering of the proposed STO with various numbers of constrictions.

CHAPTER 2

DESIGN AND FABRICATION OF CONSTRICTED GEOMETRY

2-1. Device Design

Design parameters were set to meet two of the following criteria. First, the narrowest part of the nanowire must have a width smaller than 500nm, the critical dimension to suppress four magnon scattering. For our experiment, we chose the narrowest point of the wire as 200nm and widest point as 800nm. Because we designed the shape of nanowire to be sinusoidal on each edge, the average width of the total device was 500nm. The second design parameter was the distance between the constrictions. As indicated from previous work, both the bulk and the edge modes have geometry related properties due to spin wave reflection from the metal contacts at each end of the wire. To further study such effects we designed devices that terminate in a flare-out to a wide-end (device 5) and a constricted-end (device 1-3).

The varied number of constrictions was designed to test the distance at which mutual phase locking occurs. From previous studies, mutual phase locking has been observed in STOs that were separated by several hundred nanometers [45,46] and up to 1000 nm was recently predicted for oscillators that use directional spin wave beams [49–52]. Because the separation for phase locking is not known for spin Hall oscillators, we have used 600nm, 900nm and 1800nm for the spacing, which is similar to the range was used in previous works.

As a result of this criteria, our design includes nanowires with a different number of constrictions per wire. Because the length of the wire is kept constant for samples with a different number of constrictions, the distance between constrictions varies

accordingly. Fig 2.1 illustrates the full spectrum of designs which were used for the experiment.

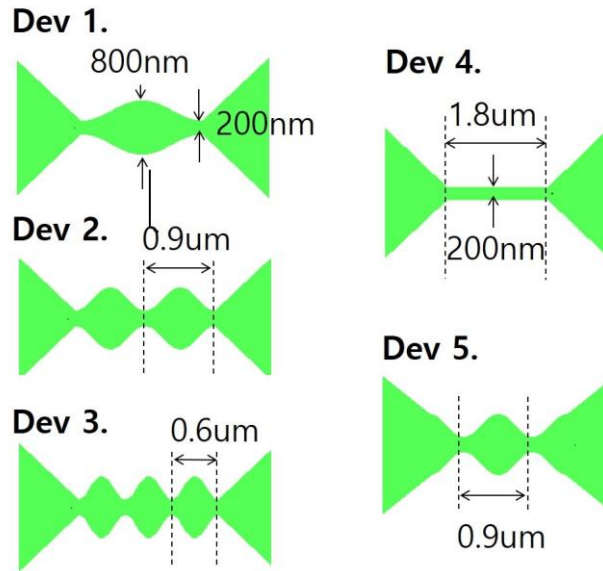


Fig 2.1 Device designs

It can be seen from the fig 2.2 that an additional flare out that extends from the nanowire was also included in the design to reduce the effect of nanowire being asymmetric.

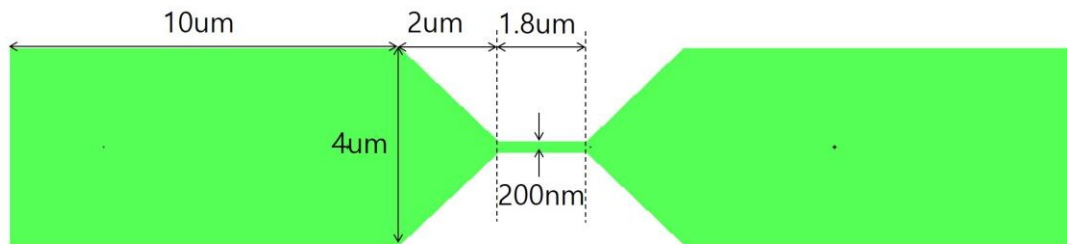


Fig 2.2 Design of the flare-out

Because the electrical signal that we plan to measure is at high frequency, metallic contact electrodes were designed to have a waveguide impedance of 50 ohms. Another

consideration was to make the contacts symmetric about the nanowire axis because asymmetric electrodes can be a source of spurious Oersted field that influences the magnetic response of the devices.

2-2. Fabrication Methods

The thickness of the CoFeB and Pt was 4nm for both of the layers. Recent studies on the effect of the interface on the ferromagnetic layer and Pt suggested that the presence of an additional layer can improve the effective spin Hall angle [53–55]. Accordingly, we inserted a 0.3nm of Hf spacer between CoFeB and Pt layer. CoFeB has a larger saturation magnetization and a smaller anisotropic magnetoresistance compared to permalloy (Py), which leads to a higher critical current and smaller resonance signals for STFMR and auto-oscillations. However, we selected CoFeB over Py (which is usually used for spin Hall geometry) because the higher saturation magnetization of CoFeB also leads to a higher oscillation frequency as expected from equation (1.6). The layers were grown in the Buhrman group AJA sputtering system at room temperature.

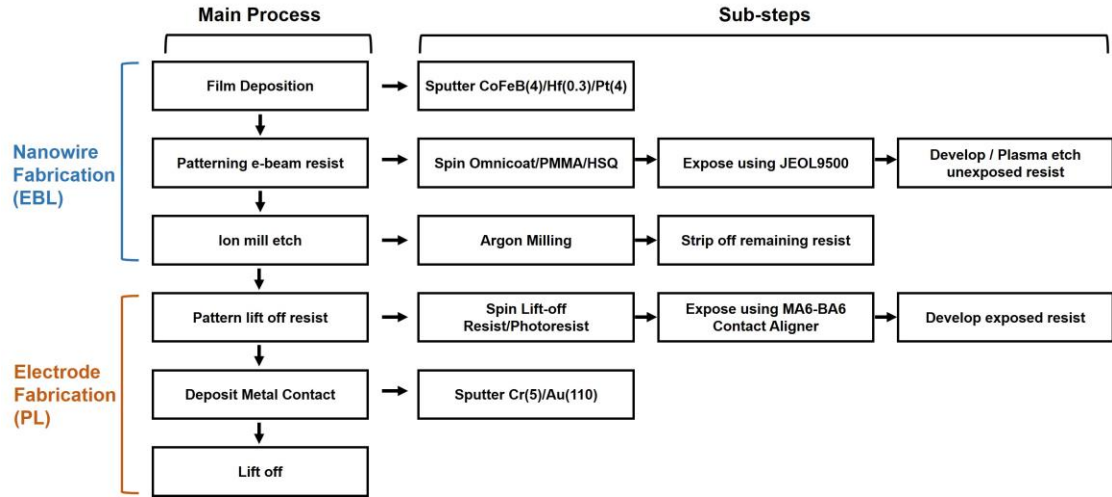


Fig 2-3. Fabrication process flow diagram for the fabrication of the spin Hall nanowire with constricted geometry

The fabrication process carried out as on the flow chart in Fig 2-3. Nanofabrication of the spin Hall nanowire was done using a combination of the electron-beam lithography and ion milling to pattern the nanowires [56], and photolithography [57] to fabricate the large electrode patterns.

We used a bilayer of 6% HSQ (XR-1541) negative tone e-beam resist and 4% 495K PMMA as an ion mill mask. Multiple chemical layers were spun with a spin coater at the Cornell Nanofabrication Facility (CNF). The first layer on the bottom is an omnicoat which allows better adhesion of PMMA to the substrate, and it makes stripping off of the chemical layers easier after milling. Then PMMA, which is known to have low etching rate to argon ion bombardment, was spun at 2000 rpm for 120 seconds. Finally, negative tone e-beam resist was spun at 2000 rpm for 60 seconds. After the e-beam resist stack was ready, the wafer was exposed to an e-beam using the JEOL 9500 e-beam lithography tool. The dose test was done to find the dosage that optimize the feature size of the samples. Dosage from $800\text{uC}/\text{cm}^2$ to $2000\text{uC}/\text{cm}^2$ were tested and the resulting features were measured with a scanning electron microscope (SEM). We found that the $800\text{uC}/\text{cm}^2$ dosage resulted in a narrowing of the features

while the 2000 uC/cm^2 nanowire was wider than desired. We used a dosage of 1500 uC/cm^2 to pattern devices used for our experiment.

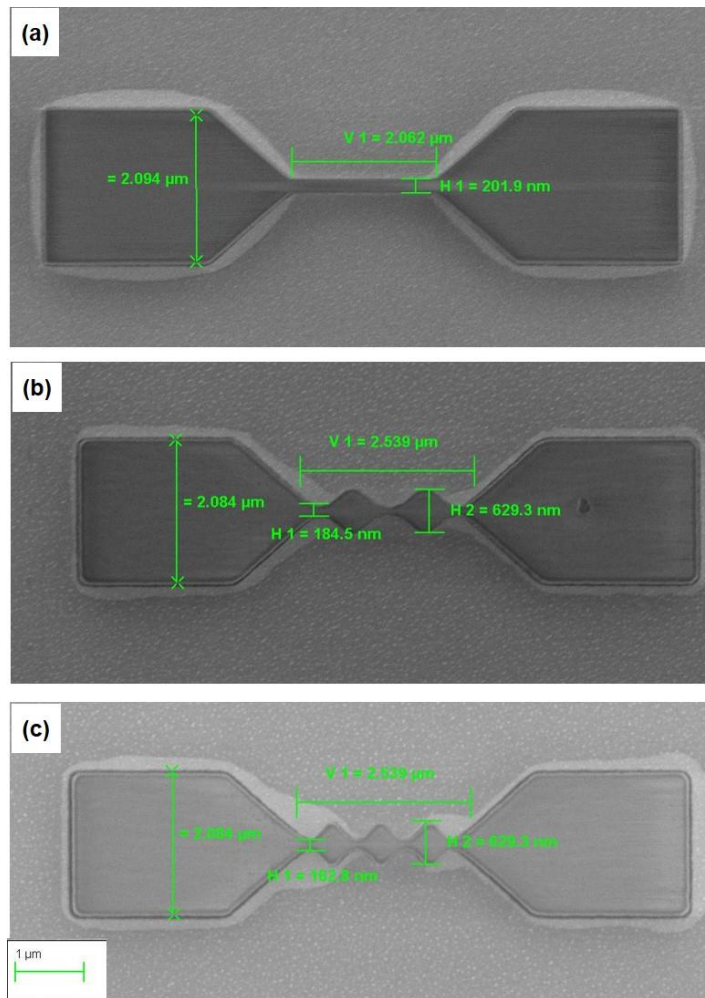


Fig 2-4. SEM Image of fabricated device for (a) simple nanowire with $1.8 \mu\text{m}$ length and 200 nm width, and constricted nanowires with (b) 900 nm and (c) 600 nm spacing. Dosages were 2000 uC/cm^2 for (a) and 800 uC/cm^2 for (b) and (c). The flare-out design is different from Fig 2-2 as the SEM images were taken for earlier version with the different flare-out design. The rest of the design and the e-beam process were the same as devices used for characterization.

After e-beam patterning we etched away the unexposed e-beam resist using an oxygen plasma in the Oxford 80 etcher with a 50mTorr pressure, a 20 sccm oxygen

rate, and a 100 W power. A total of 1 min 30 sec of etching time was necessary to fully etch the unexposed resist.

For etching the metal layers uncovered by the e-beam resist, we used the AJA argon ion mill. Because PMMA was used for the mill mask, 30 seconds of milling was enough to fully etch the metal without damaging the patterned features. It is empirically known that typical resists become stubborn after ion milling, therefore we sonicated at 60 C in 1195 remover to remove of the resist mask after ion milling.

For the photolithography of the electrodes we used the MA6 contact aligner. The mask was fabricated with the Heidelberg DWL2000. Because we used the lift-off technique for the photolithography, we spun a double layer of lift-off resist and Shipley 1813 positive tone photoresist. After exposing for 4.3 seconds, we developed for 60 seconds in MIF726. Then we deposited the 110 nm Au electrode layer over a 10nm of Ti adhesion layer. The metal layers were deposited in CCMR 3-gun target magnetron sputter system. For the lift-off, the wafer was sonicated in acetone for 5 minutes. Finally, we diced each die using the DISCO saw at CNF.

CHAPTER 3

CHARACTERIZATION METHODS

3-1. Spin Torque Ferromagnetic Resonance

Principle of STFMR

Spin-torque ferromagnetic resonance (STFMR) was developed to electrically measure the magnetic resonance excited by an ac electric signal. It was first developed to experimentally study the vector direction and the magnitude of spin-transfer torques in spin valves and magnetic tunnel junctions [58–61].

Recently, Liu *et al.* [25] has shown that the same principle can be used to find the spin torque vector for ferromagnet/spin Hall metal bilayer films. Because the oscillating spin current is injected from spin Hall metal to the ferromagnet, it applies an oscillating spin-torque on the magnetization. At the ferromagnetic resonance condition, the resulting oscillation of magnetization results in an ac resistance oscillation of the bilayer through the anisotropic magnetoresistance. Since the applied current is also oscillating at the same frequency, a dc voltage is rectified through the mixing of ac current and ac resistance. Thus, if we sweep the frequency of the ac current that we apply, a dc voltage will appear when the resonance frequency of magnetization oscillation matches with the swept frequency.

Figure 3-1 shows the mixing signal that results from spin torque FMR in a normal extended film [25]. The overall mixing signal can be represented by $V_{mix} = I_{RF} \Delta R_{RF} \cos\varphi/2$ where I_{RF} , ΔR_{RF} and φ is rf current, ac resistance variation and the phase offset between the current drive and the magnetic response, respectively. Since φ has a dependence on the driving torques and the frequency detuning, the mixing signal appears as combination of symmetric and antisymmetric Lorentzians

that depend on the direction of the total torque. To make this clear we can include the field dependent precessional phase $\phi(H)$ in the phase offset. Thus equation can be rewritten as

$$V_{mix} = I_{RF} \Delta R_{RF} \cos(\varphi - \phi(H)) / 2 \quad (3.1)$$

Using the trigonometric identity this becomes

$$\begin{aligned} V_{mix} &= \frac{I_{RF} \Delta R_{RF}}{2} [\cos(\varphi) \cos(\phi(H)) + \sin(\varphi) \sin(\phi(H))] \\ &= \frac{I_{RF} \Delta R_{RF}}{2} [\chi'(H) \cos(\varphi) + \chi''(H) \sin(\varphi)] \end{aligned} \quad (3.2)$$

We have used the relations $\chi'(H) = \cos \phi(H)$ and $\chi''(H) = \sin \phi(H)$, where $\chi'(H)$ and $\chi''(H)$ are the real and imaginary parts of dynamic susceptibility functions that derives from linearized LLG equation [62]. Because $\chi'(H)$ and $\chi''(H)$ is proportional to symmetric and antisymmetric Lorentzians, respectively [63], we can see that in case of in-plane driving field without spin torque (when the FMR phase and the rf current phase have difference of 90°), χ' term vanishes and mixing voltage is only proportional to antisymmetric Lorentzian. Similarly, if we can have only the spin torque, FMR phase and rf current phase will have difference of 0° and mixing voltage will show a symmetric spectral line shape. The symmetric and antisymmetric terms of mixing signal presented as Lorentzian and its derivative as can be seen from Fig 3-1 (b) and (c).

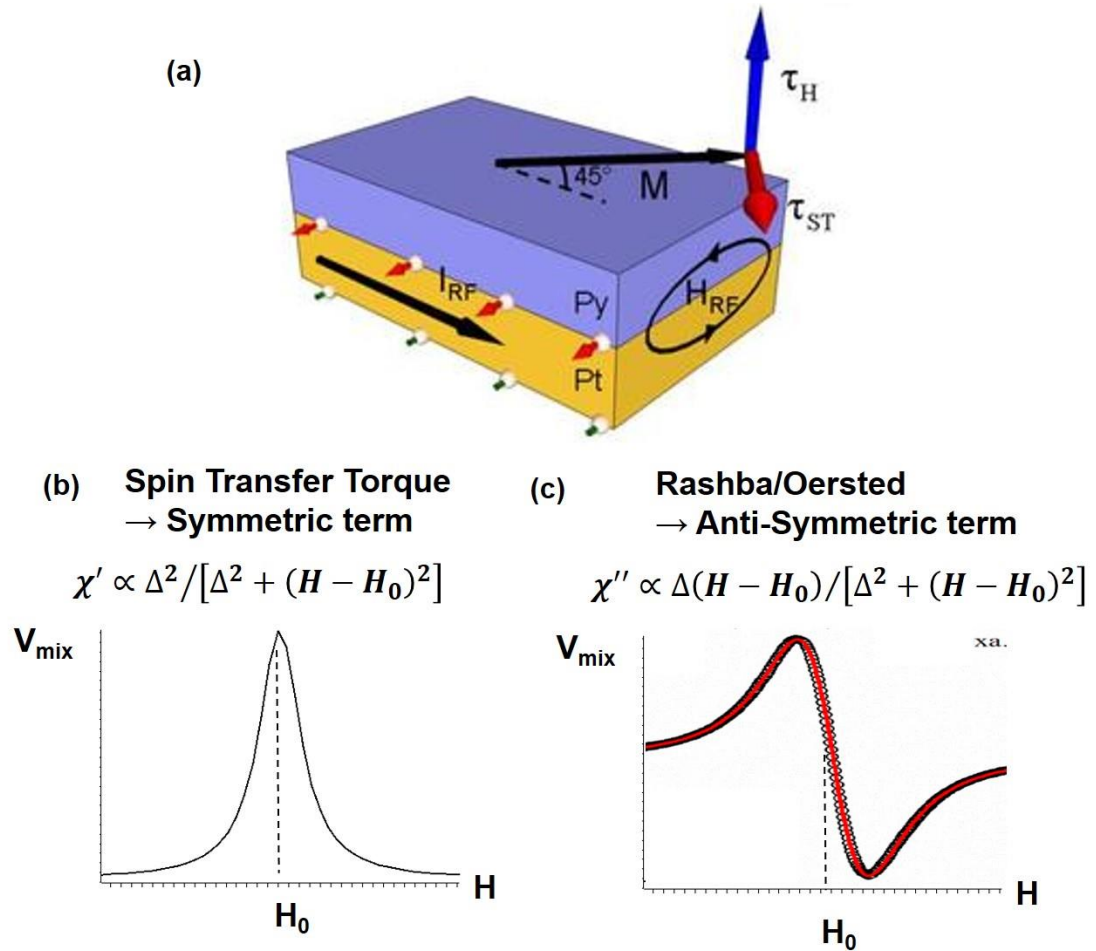


Fig 3-1. (a) STFMR schematics [25]. The mixing voltage is a linear combination of (b) symmetric and (c) antisymmetric component. Δ and H_0 refers to linewidth and resonant field, respectively.

Experimental setup

Because we perform our experiment with high-frequency microwaves, the connection between the sample and the measuring apparatus plays an important role. In our case, the sample was mounted in a brass box with mounting wax and wire-bonded (using TPT wire bonder) to the coplanar waveguide (CPW) in the brass box. For the high-frequency circuit elements, SMA-connected coaxial cables were used to minimize loss. The sample box is held between the magnet poles and a field modulation coil.

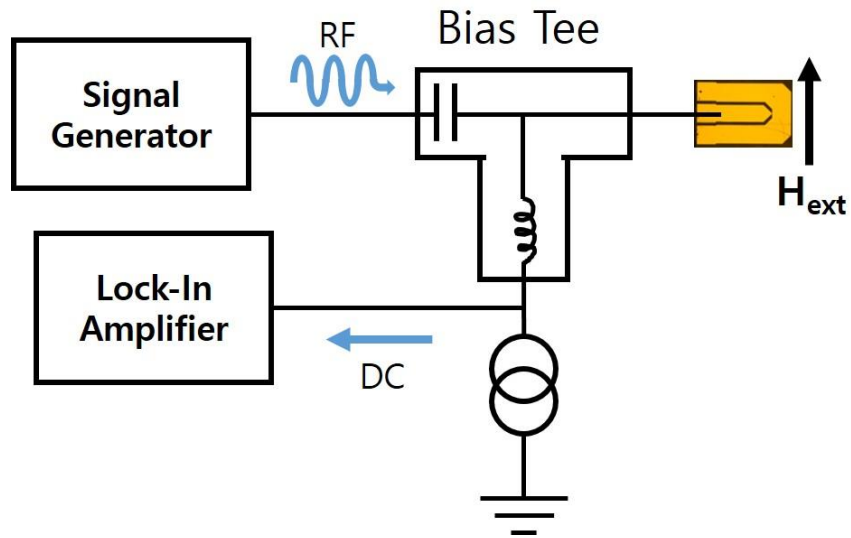


Fig 3-2. Microwave circuitry for the STFMR measurement

The microwave circuit for the STFMR measurement consists of a microwave signal generator to apply an ac electrical signal to a sample and a lock-in amplifier to measure the resultant voltage. We have connected the sample to the microwave line using a bias-tee to separate the ac excitation from the resulting dc voltage. A high-accuracy current source (Keithley 2400) was connected to the dc side of the bias-tee to enable measurement of the dc current bias dependence of the resonance.

3.2 Heterodyne Spectrum Analyzer

The basic philosophy of measuring an auto-oscillation signal is much simpler than STFMR. Since our sample generates an ac signal, we merely have to measure it using a spectrum analyzer. The caveat is that the signal is often small and hard to find without prior knowledge of its frequency at a particular magnetic field. We have built our own heterodyne spectrum analyzer, which we can optimize for the frequency

range of interest and the resolution bandwidth. We have used microwave circuit components from various vendors for that purpose.

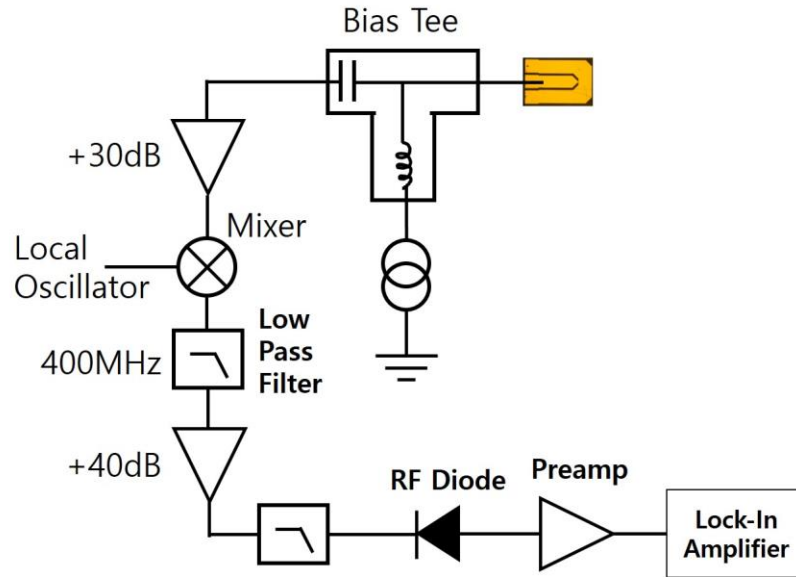


Fig 3-3. Schematics of the microwave circuitry for home-built spectrum analyzer used in this experiment.

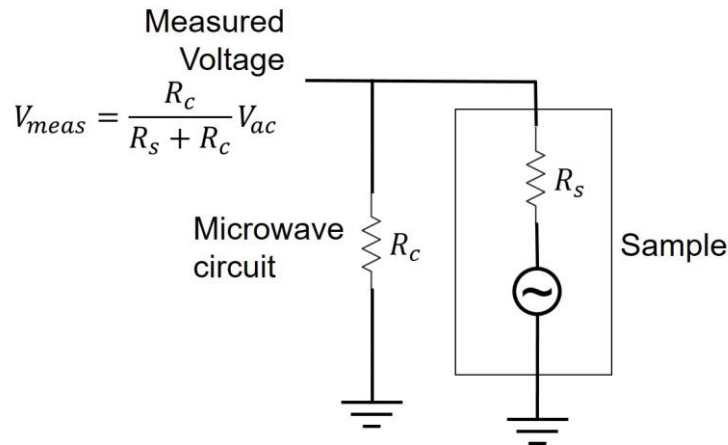


Fig 3-4. Circuit diagram of the sample and the microwave circuit. R_s and R_c refers to the resistance of the sample and the input resistance of the microwave circuit seen from the sample side, respectively.

It should be noted that there is a difference in impedance between the nanowire and the microwave transmission line. The resistance of a typical nanowire was 700 to 900

Ω . Since the input resistance of the measurement device is 50Ω , most of the voltage is actually applied to internal resistance of the sample. The ratio of measured voltage to actual voltage generated by the auto-oscillation can be calculated by the simple voltage divider equation.

The first part of the heterodyne spectrum analyzer is composed of amplifiers that amplify the signal from the sample and a bias-tee to apply dc current to the sample without affecting the ac signal which comes out of it. The amplified signal then goes into a mixer. The output signal contains a product of the input signal and the local oscillator. Assuming that each signal is sinusoidal (or is composed of sinusoidal waves), the output contains spectral components with frequency f_1+f_2 and f_1-f_2 where f_1 is the frequency of signal from the sample and f_2 is the output frequency of the local oscillator. We used an Agilent E8257D signal generator as a local oscillator, which has a widely tunable frequency and power range. After mixing, we filter out the higher frequency component with a low pass filter with 400 MHz cut-off frequency. The latter part of the spectrum analyzer is composed of a circuit which amplifies and then filters out the highest frequency components to determine the resolution bandwidth of the whole system. Because we were using a lock-in amplifier, an RF diode is used to convert the RF power into voltage. Finally, the voltage signal was amplified using Stanford Research SR560 preamplifier and measured using lock-in.

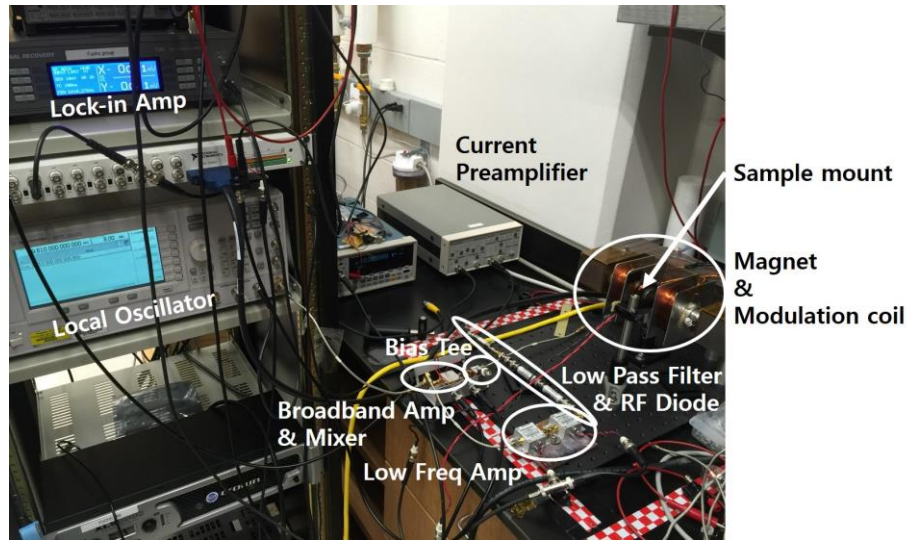


Fig 3-5. Photograph of the experimental setup for the heterodyne spectrum analyzer

In most of the cases when a magnetic signal is buried in spurious signals of non-magnetic origin, magnetic field modulation can be used to get a better signal to noise ratio [64]. To do this we have used a small modulation coil that was installed next to the electromagnet pole ends. The coil was connected to an oscillator source of a lock-in amplifier. An audio-amplifier was used to drive the low resistance coils. When we use field modulation what we measure is the change of the voltage with respect to the change of the small magnetic field modulation, which is effectively the derivative of the original signal with respect to magnetic field. Thus the obtained data are integrated over magnetic field, converting a derivative Lorentzian line shape into the Lorentzian line shape that we expect. The detailed procedure is discussed in the next subsection.

3.3 Calculation of Power Spectral Density

Characterizing the power output of our STOs is important for quantifying their behavior. Since our spectrum analyzer records lock-in voltage, we need to calibrate it

to convert voltage to power spectral density (pW/GHz). We have calibrated the output power and conversion factors using following procedure.

It should be noted that power spectral density measures a power intensity in the frequency domain. When using a spectrum analyzer, if total power is calculated at each frequency, the measurement will give totally different results depending on the resolution bandwidth used. Therefore, for a random signal with unknown bandwidth and properties, it is useful to use the unit which is defined as per frequency unit. Thus, to obtain the total power from the signal, power spectral density has to be multiplied by the bin width and then integrated over frequency.

First we calibrated the output power using Johnson noise because it can be related to fundamental constants. Since the thermal noise is white it has a flat spectrum. By comparing the lock-in voltage of a 50 Ω reference resistor at two different temperatures, we can get a relationship between voltage and power as a function of frequency. The one sided power spectral density from the Johnson noise is given by

$$PSD = k_B T \quad (3.3)$$

where PSD , k_B and T represent the power spectral density of Johnson noise, Boltzmann constant and the temperature in Kelvin, respectively. Assuming that everything is in thermal equilibrium, the temperature difference between the reference resistor measured at room temperature and in the liquid nitrogen is

$$\Delta T = 300 - 77 = 223K, \quad (3.4)$$

thus

$$\Delta PSD = k_B \Delta T = 3.077 \frac{pW}{GHz} \quad (3.5)$$

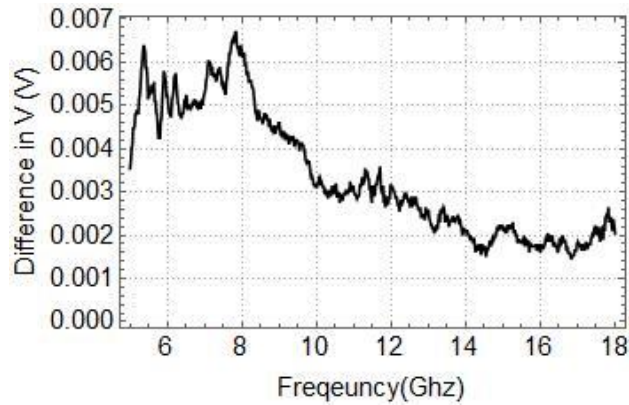


Fig 3-6. Difference in lock-in voltage for 50 Ohm termination at room temperature and in the liquid nitrogen temperature as a function of frequency

From our measurements of the 50 Ω reference resistor, and after subtracting the voltage that we obtained from the liquid nitrogen temperature to room temperature, we find the difference in lock-in voltage from Johnson noise as given in Fig 3-6. Because we used a flexible SMA cable which has higher attenuation than the cables that we used in other microwave circuits, we separately characterized its frequency dependent attenuation using a vector network analyzer (VNA), and used the result to correct our Johnson noise measurement.

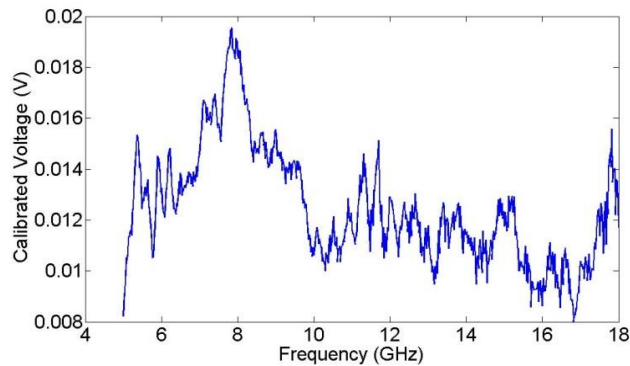


Fig 3-7. Difference in lock-in voltage for 50 Ohm termination at room temperature and in the liquid nitrogen temperature as a function of frequency after taking the cable attenuation into account

The corrected voltage difference between the Johnson noise at 300 K and 77 K is shown in Fig 3-7. The Johnson noise signal became flatter after we took the cable attenuation into account. We found that the conversion rate (pW/GHz)/Lock-in-mV was roughly 1/4. A frequency dependent conversion rate for PSD (pW/GHz) to lock-in-voltage (mV) ratio as a function of frequency is presented in Fig 3-8.

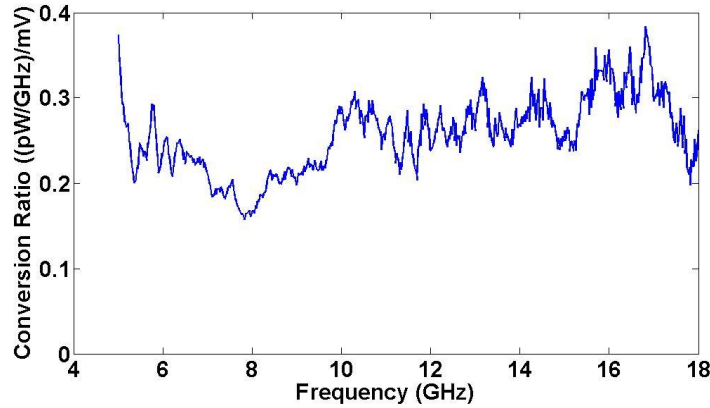


Fig 3-8. Conversion rate for PSD-to-lock-in-voltage ratio as a function of frequency

Since we used field modulation to obtain the auto-oscillation signal, the data we get is actually dV/dH . To compute the total power density, we need to integrate the signal with respect to magnetic field. However, since we swept frequency in our measurement, we are not able to directly integrate with respect to field. Therefore we used following equation to calculate the total lock-in voltage at a given frequency and then converted it to the power spectral density.

$$V(f) = \int \frac{dV(f)}{dH} \frac{dH(f)}{df} df \quad (3.6)$$

As it can be seen from fig 3-9 (a), dV/dH is the raw data that we get directly from the lock-in amplifier. dH/df can be obtained from the data by dividing the difference in

resonance field between adjacent peaks by the difference in frequency. Because the resonance follows the trend of the Kittel formula, we can also fit the resonance frequencies to the Kittel curve and take a derivative. The first method was used to obtain the integrated data on fig 3-9 (b). It can be seen that noise was observed in the raw data and that contributes to the signal, such that when it is integrated, the baseline (where there are no resonances) is not flat. The same method was used to get the experiment results in chapter 4.

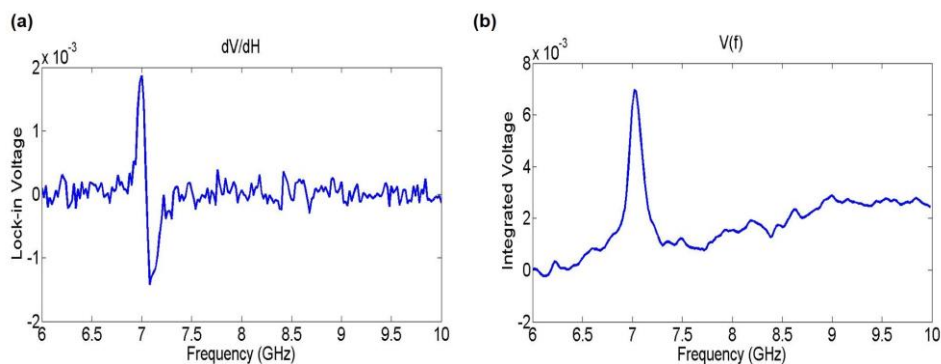


Fig 3-9. (a) Raw data for the auto-oscillation obtained from the lock-in amplifier in presence of field modulation and (b) the integrated data. The auto-oscillation is from device 3 under 400 G of applied field.

CHAPTER 4

RESULTS AND ANALYSIS

4-1. STFMR Results

For samples with multiple constrictions, the features in STFMR signal are not as easy to explain as that of the extended thin film. We have exclusively obtained data from a device with the least number of constrictions (Device 1 from Fig 2-1) and a device with the most constrictions (Device 3 from Fig 2-1). First we consider the data obtained from device 1, which has two constrictions at the end of the nanowire and one large extended middle. Instead of the sweeping frequency of the ac current, we swept the magnetic field applied on the sample. Because we took measurements at frequencies between 6 GHz to 12 GHz with a 0.25 GHz step, we were able to obtain the data that is essentially the same as what we would have obtained with frequency sweep.

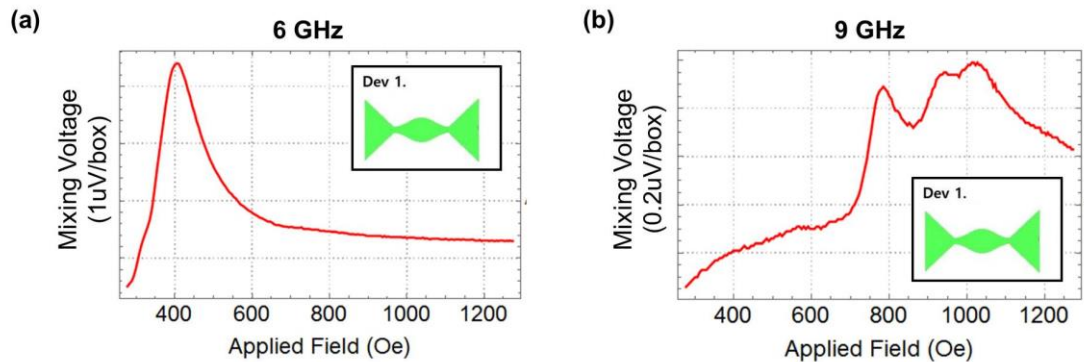


Fig 4-1. STFMR signal for a device with two constrictions at (a) 6 GHz frequency and (b) 9 GHz frequency. Multiple peaks are observed at higher frequency.

From Fig 4.1 we can see that at low frequency, around 6 GHz, there is only one resonance peak at a magnetic field of ≈ 400 G. As the frequency is increased, we see more features emerge. Starting from 9 GHz, we see evidence of two peaks, at 750 G and 1000 G. The continuous appearance of the resonance peak indicates that these resonances are likely unresolved at low field/frequency but split apart at higher field/frequency. The full trend of spectrum of STFMR data can be seen on Fig 4-2. The magnitude of the signal was normalized.

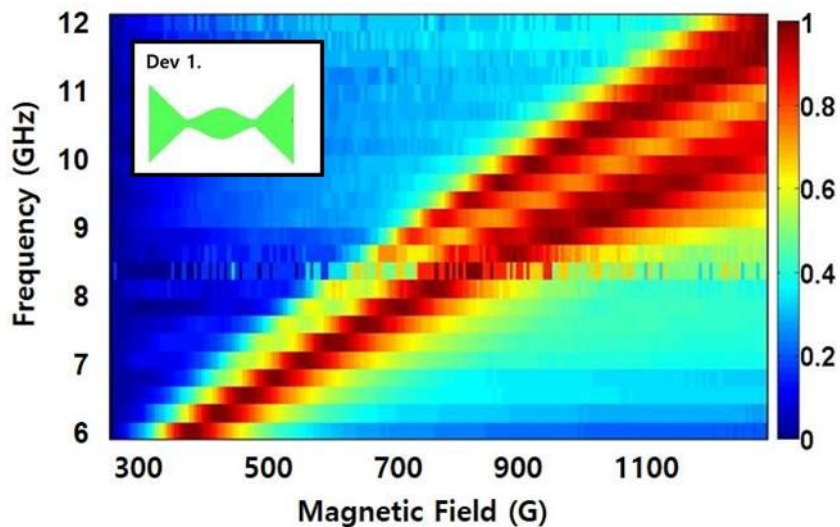


Fig 4-2. Full trend of spectrum of STFMR from 6 GHz to 12 GHz for device 1. Data are normalized to show clear trend of the peaks. Maximum mixing voltage and minimum mixing voltage were mapped to 1 and 0, respectively.

We observe different behavior in how peaks form in the sample with more constrictions, as it can be seen from Fig. 4-3. In case of the sample with four constrictions and 3 extended parts (device 3), we first see the behavior that is similar to the previous case (with small number of constrictions), where at lower frequency a single dominant peak appears near 300 G. But as we increase the frequency, rather than splitting of one peak into several peaks, we observe the appearance of new peaks

at low magnetic field. To be more specific, at 6 GHz there is a single resonance at 290 G. When the frequency is increased to 8 GHz, we see another peak appearing at 270 G in addition to the large peak that now appears at 510 G. As we increase the frequency further, we see total 3 peaks at frequency of 9.25 GHz at 270 G, 380 G, and 690 G, respectively.

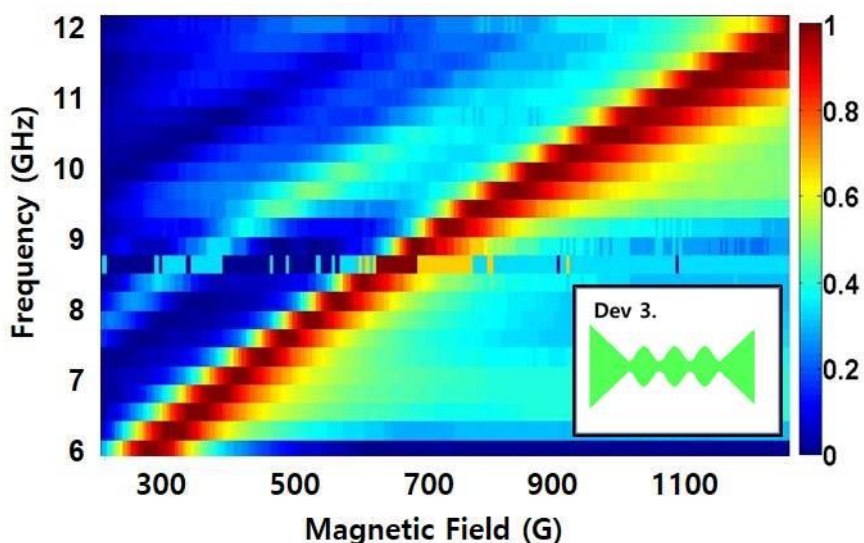


Fig 4-3. Full trend of spectrum of STFMR from 6 GHz to 12 GHz for device 3. Data were normalized in a similar fashion with Fig 4-2.

4-2. *STFMR Analysis*

For an extended ferromagnetic film, it is known that STFMR does not show a significant difference for different angles of applied magnetic field [25]. Whereas for nanowires, due to its anisotropic geometry, angular dependence of a signal can be naturally anticipated [5]. Our sample has a non-trivial geometry including extended and confined parts, and thus new behaviors of the STFMR signal was expected. Since the apparatus lacked a capability to tilt the sample and accurately measure the angle,

we were only able to get data for magnetic field applied at $\approx 45^\circ$ and at $\approx 85^\circ$ with respect to the nanowire axis.

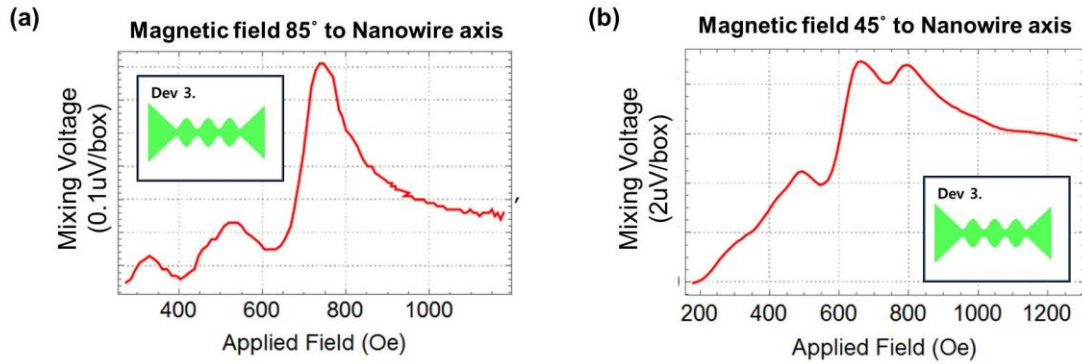


Fig 4-4. Comparison of STFM R for magnetic field applied at (a) $\approx 85^\circ$ and (b) $\approx 45^\circ$ with respect to nanowire axis. Both data were taken at rf frequency of 9 GHz.

Fig 4-4 (a) shows a signal obtained with an 85° field angle for device 3 at 9 GHz frequency. We can observe from figure 4-4 (a) that the most dominant peak appears at 750G when magnetic field is almost perpendicular to nanowire axis. On the other hand figure 4-4 (b) shows that when the magnetic field is applied at 45° , two separate peaks appear at 660G and 800G. Because the mid-point magnetic field of two peaks we observe at 45° are the same as the field of the dominant peak at 85° , we suspect that the tilting the angle of the magnetic field results in a splitting of the peak. The physical reason for the splitting is not yet clear, however, we tentatively attribute it as coming from the edge of the nanowire. Unlike the case when magnetic field is perpendicular, at 45° , a larger area of the nanowire edge experience the perpendicular magnetic field. This will result in a larger response from the edge region, and thus we might expect to see a larger signal.

The second evidence that the peak splitting is due to an edge effect comes from its current dependent behavior. When the current was flowing in negative direction (anti-damping) the relative magnitude of the peak was less dependent on magnitude of

current. However, when the current flows in positive direction, the peak quickly diminishes. Because the edge mode has a stronger dependence on current than the bulk mode, this can be considered as evidence that we are seeing a larger edge contribution when we tilt the magnetic field angle.

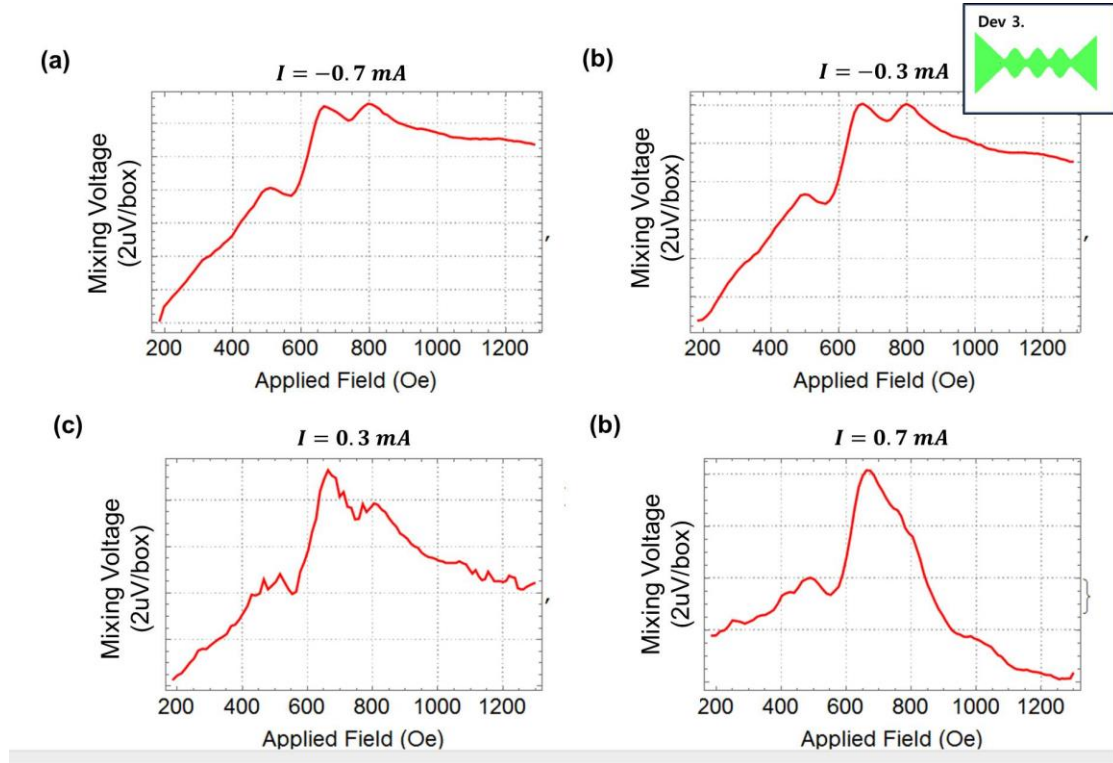


Fig 4-5. Current dependence of STFMR resonance signal for magnetic field applied at 45°. The data was taken from device 3 at 9 GHz.

4-3. Auto-Oscillation Properties

Auto-oscillation data were obtained by using the spectrum analyzer discussed in section 3-2. For auto-oscillation measurements, the frequency was swept at various, fixed magnetic field values. The power spectrum was obtained as a function of frequency and magnetic field following the procedure from section 3-3.

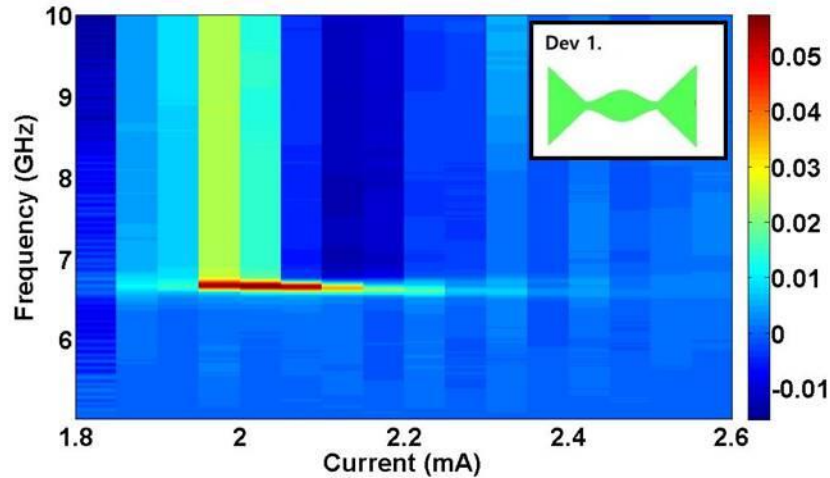


Fig 4-6. Current dependence of an auto-oscillation signal. We can see that the integrated lock-in voltage is maximum at $I=2\text{mA}$ of driving current. For $I>2.25\text{mA}$, the peak reduce in intensity and split to two peaks.

First we show the current dependence of the output spectrum in Fig 4-6 for the sample with the least constriction (Dev 1). Since auto-oscillations occur only when the natural damping is cancelled by a spin transfer torque, there is a critical current density threshold. In our experiment, we were able to start observing auto-oscillations at a current of 1.8 mA, which corresponds to a current density of $4.5 \times 10^8 \text{ A/cm}^2$ at the 200 nm constriction (and 4 nm thickness). An assumption that we used was that the resistivity difference between the CoFeB and Pt is large enough that we can consider most of the current to be flowing through Pt rather than CoFeB. This critical current is very high, and close to the electromigration current of Pt. Accordingly, we observed a gradual increase in the overall resistance of the sample, possibly due to electromigration. The current where maximum power signal was found was 2 mA for magnetic field of 520 Oe, where the maximum PSD was 10 pW/GHz. When current density is too high, the signal again decays. Right before the signal became too small to detect we were able to observe a splitting of two peaks in 2.25 to 2.5mA region.

The similar effect of splitting peaks was observed at high current density by Demidov *et al.* [10] and was attributed as the multimodal oscillation regime.

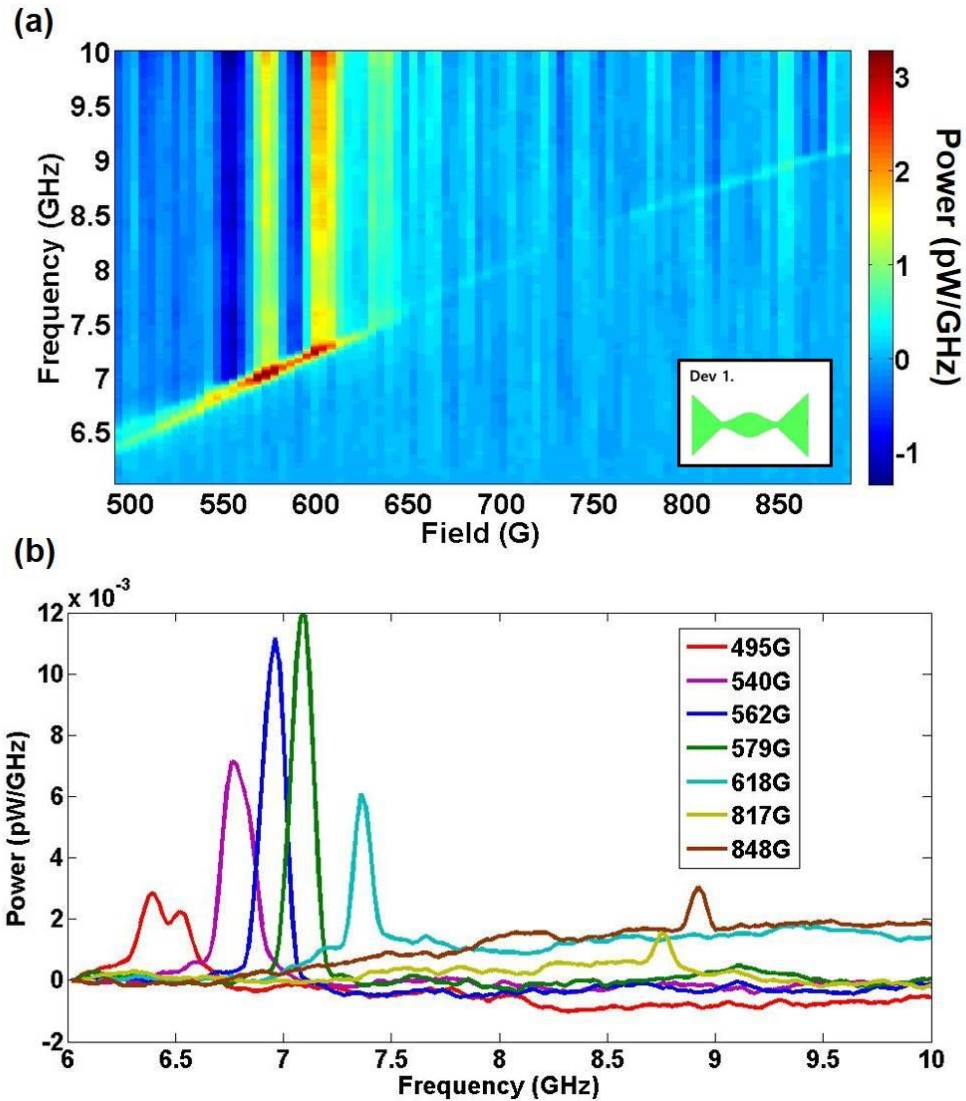


Fig 4-7. Magnetic field dependence of an auto-oscillation for device 1. Since the signal is integrated after measurement, figure (a) shows a remnant tail at high frequency for certain magnetic field. The linecuts are shown in (b) to better show individual spectra.

From Fig 4-7 we can see the magnetic field dependence of auto-oscillation for sample device 1. Under a 2.15 mA current, the maximum power was obtained near

560 G, with oscillation frequency of 7 GHz and a power of 2.5 pW/GHz. It can be noted that the peak power spectral density is small compared to the observations of Duan *et al.* [5] or Demidov *et al.* [10]. However, there are two factors that should be considered in this result. First, we need to consider the effect from impedance mismatch, which was discussed in section 3-2. Since resistance of nanowire was 800 Ω and impedance of microwave circuit is 50 Ω , the actual voltage generated by the oscillator should be $50/(800+50)=17$ times the voltage measured. The second thing is the difference in the anisotropic magnetoresistance of CoFeB as compared to Py, as discussed in section 2-2.

Another important difference from the simple nanowire geometry suggested in reference [5] is the auto-oscillation modes. In figure 4-6 the number of dominant peaks remained one. The observation of a single peak, which is similar to results from reference [10], can be attributed to the fact that the current density and therefore the magnitude of the spin current is larger in the constricted than in the unconstricted regions of our device. This suggests that the auto-oscillation is above the threshold only in the constricted region of the nanowire.

4-4. Relation between auto-oscillation and STFM for constricted samples

For conventional samples with uniform width, STFM is known to give information about the magnetic modes of a sample, which can be used to predict the auto-oscillation frequencies of the device. In the case of our nano-constriction devices, this does not seem to be the case, and it differentiates the behavior of our devices from previous studies of spin hall nanowires and skewed nanowires [5,65–67].

While performing STFMR and auto-oscillation experiments we have found that there is a small but noticeable difference between resonance fields measured using STFMR and that using auto-oscillation (Fig. 4-8).

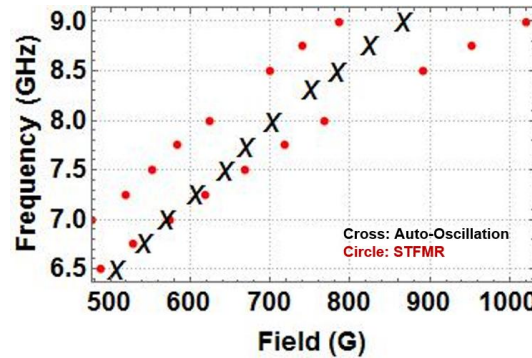


Fig 4-8. Plot of resonance peaks measured using STFMR (circle) and auto-oscillation (cross) for device 1. Two lines for STFMR are from double peaks for device 1 which were also shown in Fig 4-2.

To understand this more clearly, we made a more careful measurement of STFMR in which we vary the dc current. The anti-damping torque increases proportional to the dc current density, and this in turn increases the average precessional angle of magnetization. To keep the angle constant we decrease the rf current as we increase the dc current as indicated on figure 4-9. The measurement was coarsely sampled for higher ac power for the current below 1.5 mA and densely sampled near the 1.8 mA threshold for auto-oscillations.

The STFMR results for a 9 GHz drive are shown in figure 4-9. As we reduce the rf current and approach the threshold, the STFMR starts to resemble the auto-oscillation spectrum. At the point where dc current exceeds the critical threshold, a unique peak emerges at 874 G, which is identical to the magnetic field where we observed an auto-oscillation peak at 9 GHz. This indicates that for nano-constricted samples with multiple constrictions, the zero current resonance peak from the STFMR is not necessarily a precursor to an auto-oscillation. We can see from these results that STFMR excites all modes both in the wide and the narrow region of the nanowire. On

the other hand, pure auto-oscillations only occur in above the threshold region and can be different from the modes which appeared to be dominant from the STFMR.

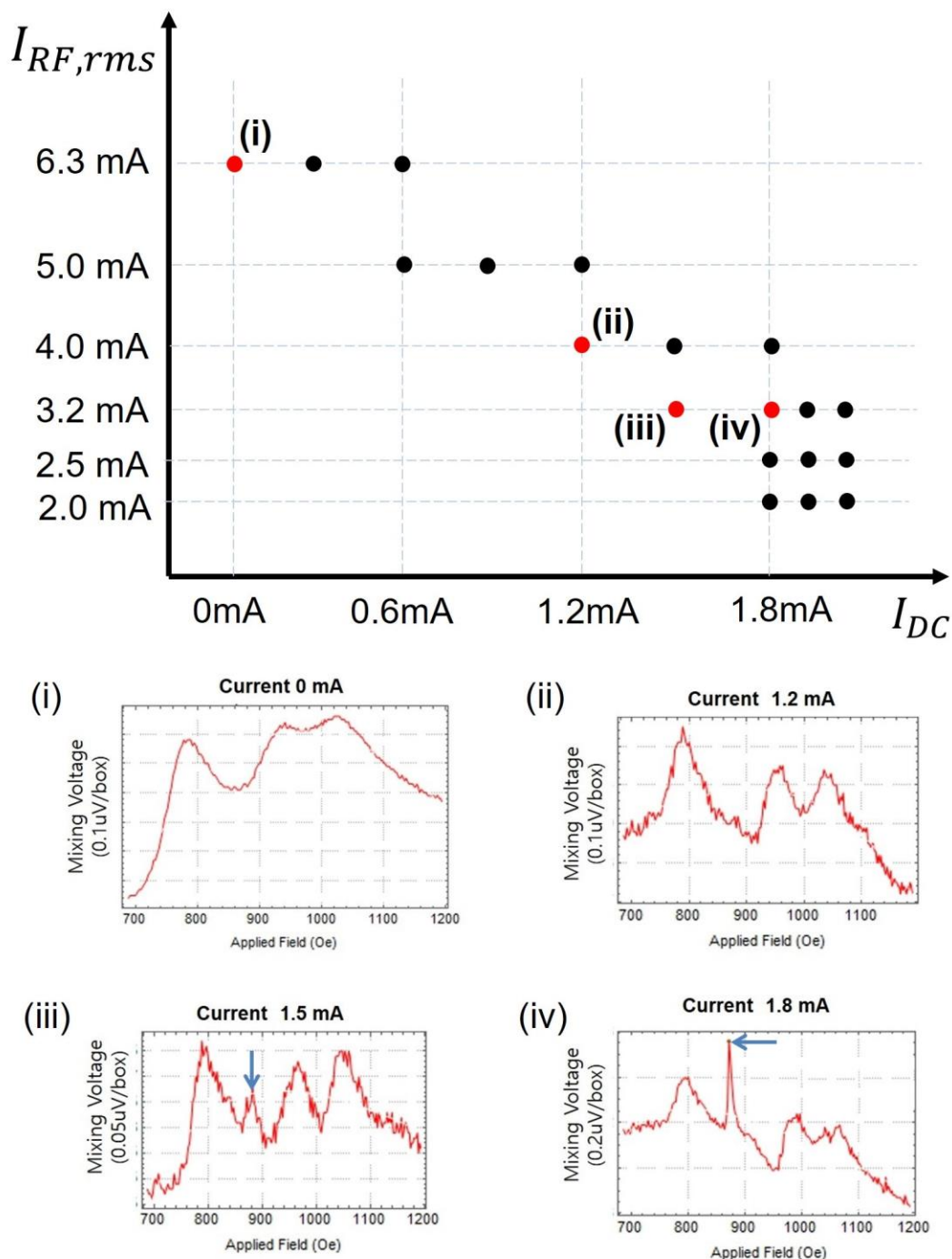


Fig 4-9. Rf current and dc current configurations for analyzing the current dependence of STFMR. (i), (ii), (iii), and (iv) show STFMR spectra at specific points indicated on the graph by a red dot. At current of 1.8mA we see a sharp peak which coincide with auto-oscillation signal but distinctive from other resonant peaks

CHAPTER 5

CONCLUDING REMARKS

Because the data presented here clearly shows both ferromagnetic resonance and auto-oscillations, we can take this result as a stepping stone toward understanding and optimizing the spin dynamics in spin Hall oscillator devices with non-trivial geometry for practical purposes.

Angle dependent measurement.

As indicated from the previous results [5,10], the spin dynamics of nano-size samples depend strongly on the angle between the magnetic field, the current direction and the dimensions of the sample. For instance, from Duan *et al.* [5], it is shown that as the angle of the magnetic field changes only by 5° , the strength of different modes of the oscillation can be changed by a large amount.

Although we have seen clear auto-oscillation signals near an angle of $\approx 90^\circ$ between the nanowire axis and the magnetic field direction, the exact angle was not obtainable due to a limitation of the apparatus. The strong dependence of the output power on the angle offers a chance for our device to have higher power output at an optimized angle. In addition, as seen in the STFMR results, our device has additional magnetic resonances when the angle between nanowire and the magnetic field is smaller. Identifying the origins of this phenomenon will be easier once we have better control over the field angle.

Micromagnetic simulation of the device.

Although we have characterized the ferromagnetic resonance and auto-oscillation in our samples, the origin of the different peaks and mechanisms related to geometry are

not clearly understood. To explain our findings better, micromagnetic simulation will be a very useful tool. Using micromagnetic simulations, we hope to extract the spatial modes that correspond with our signals, and also discover the relationship between modes.

To simulate the resonance behavior we can use ringdown simulations, where we apply a magnetic field pulse and observe how the magnetization reacts. Simulation of auto-oscillations can be done by including the spin-transfer torque from the spin Hall effect. However, effort is required because the current density will vary along the length of the nanowire which will complicate implementing the simulation.

In conclusion, we have established a way to fabricate nano-constrictions using the e-beam lithography and the photolithography facilities at CNF. The magnetic resonance and the auto-oscillation properties of these devices were characterized. We found that the magnetic resonance response of these multiple constriction samples is different from both spin Hall nanowires and extended films. It has a more complicated mode structure that needs further study, including more measurements of different samples and micromagnetic simulation studies.

Auto-oscillations of nanowires with constricted regions also casts an interesting possibility for mutual phase locking. It was found that these devices generate power that is comparable to the previously reported spin Hall oscillators, and the data are consistent with power generation mostly in the constricted region of the device. These conclusions motivate more thorough calculations and simulations to find out the effective separation between constrictions for spin-wave interference. In suitably designed and optimized devices, observing an auto-oscillation with a narrower linewidth and a higher output power will be possible.

BIBLIOGRAPHY

- [1] I. M. Miron, K. Garello, G. Gaudin, P.-J. Zermatten, M. V Costache, S. Auffret, S. Bandiera, B. Rodmacq, A. Schuhl, and P. Gambardella, “Perpendicular switching of a single ferromagnetic layer induced by in-plane current injection” *Nature* **476**, 189 (2011).
- [2] L. Liu, C.-F. Pai, Y. Li, H. W. Tseng, D. C. Ralph, and R. A. Buhrman, “Spin-Torque Switching with the Giant Spin Hall Effect of Tantalum” *Science*. **336**, 555 (2012).
- [3] J. Wunderlich, B.-G. Park, A. C. Irvine, L. P. Zarbo, E. Rozkotova, P. Nemeč, V. Novak, J. Sinova, and T. Jungwirth, “Spin Hall Effect Transistor” *Science*. **330**, 1801 (2010).
- [4] J. Wunderlich, A. C. Irvine, J. Sinova, B. G. Park, L. P. Zârbo, X. L. Xu, B. Kaestner, V. Novák, and T. Jungwirth, “Spin-injection Hall effect in a planar photovoltaic cell” *Nat. Phys.* **5**, 675 (2009).
- [5] Z. Duan, A. Smith, L. Yang, B. Youngblood, J. Lindner, V. E. Demidov, S. O. Demokritov, and I. N. Krivorotov, “Nanowire spin torque oscillator driven by spin orbit torques.” *Nat. Commun.* **5**, 5616 (2014).
- [6] V. E. Demidov, S. Urazhdin, H. Ulrichs, V. Tiberkevich, A. Slavin, D. Baither, G. Schmitz, and S. O. Demokritov, “Magnetic nano-oscillator driven by pure spin current” *Nat. Mater.* **11**, 1028 (2012).
- [7] A. Hamadeh, O. d’Allivy Kelly, C. Hahn, H. Meley, R. Bernard, A. H. Molpeceres, V. V. Naletov, M. Viret, A. Anane, V. Cros, S. O. Demokritov, J. L. Prieto, M. Muñoz, G. de Loubens, and O. Klein, “Full Control of the Spin-Wave Damping in a Magnetic Insulator Using Spin-Orbit Torque” *Phys. Rev. Lett.* **113**, 197203 (2014).

- [8] L. Liu, C.-F. Pai, D. C. Ralph, and R. A. Buhrman, “Magnetic Oscillations Driven by the Spin Hall Effect in 3-Terminal Magnetic Tunnel Junction Devices” *Phys. Rev. Lett.* **109**, 186602 (2012).
- [9] R. H. Liu, W. L. Lim, and S. Urazhdin, “Spectral Characteristics of the Microwave Emission by the Spin Hall Nano-Oscillator” *Phys. Rev. Lett.* **110**, 147601 (2013).
- [10] V. E. Demidov, S. Urazhdin, A. Zholud, A. V. Sadovnikov, and S. O. Demokritov, “Nanoconstriction-based spin-Hall nano-oscillator” *Appl. Phys. Lett.* **105**, 172410 (2014).
- [11] M. I. Dyakonov and V. I. Perel, “Current-induced spin orientation of electrons in semiconductors” *Phys. Lett. A* **35**, 459 (1971).
- [12] M. I. Dyakonov and V. I. Perel, “Possibility of orienting electron spins with current” *Sov. J. Exp. Theor. Phys.* **33**, 1053 (1971).
- [13] S. Maekawa, “Magnetism: A flood of spin current.” *Nat. Mater.* **8**, 777 (2009).
- [14] J. Sinova, S. O. Valenzuela, J. Wunderlich, C. H. Back, and T. Jungwirth, “Spin Hall effects” *Rev. Mod. Phys.* **87**, 1213 (2015).
- [15] G. Vignale, “Ten Years of Spin Hall Effect” *J. Supercond. Nov. Magn.* **23**, 3 (2010).
- [16] N. Nagaosa, J. Sinova, S. Onoda, A. H. MacDonald, and N. P. Ong, “Anomalous Hall effect” *Rev. Mod. Phys.* **82**, 1539 (2010).
- [17] J. Wunderlich, B. Kaestner, J. Sinova, and T. Jungwirth, “Experimental Observation of the Spin-Hall Effect in a Two-Dimensional Spin-Orbit Coupled Semiconductor System” *Phys. Rev. Lett.* **94**, 047204 (2005).
- [18] Y. K. Kato, “Observation of the Spin Hall Effect in Semiconductors” *Science*. **306**, 1910 (2004).
- [19] J. E. Hirsch, “Spin Hall Effect” *Phys. Rev. Lett.* **83**, 1834 (1999).
- [20] S. Zhang, “Spin Hall Effect in the Presence of Spin Diffusion” *Phys. Rev. Lett.* **85**, 393 (2000).

- [21] S. O. Valenzuela and M. Tinkham, “Direct electronic measurement of the spin Hall effect” *Nature* **442**, 176 (2006).
- [22] S. O. Valenzuela and M. Tinkham, “Electrical detection of spin currents: The spin-current induced Hall effect (invited)” *J. Appl. Phys.* **101**, 09B103 (2007).
- [23] E. Saitoh, M. Ueda, H. Miyajima, and G. Tatara, “Conversion of spin current into charge current at room temperature: Inverse spin-Hall effect” *Appl. Phys. Lett.* **88**, 182509 (2006).
- [24] T. Kimura, Y. Otani, T. Sato, S. Takahashi, and S. Maekawa, “Room-Temperature Reversible Spin Hall Effect” *Phys. Rev. Lett.* **98**, 156601 (2007).
- [25] L. Liu, T. Moriyama, D. C. Ralph, and R. A. Buhrman, “Spin-Torque Ferromagnetic Resonance Induced by the Spin Hall Effect” *Phys. Rev. Lett.* **106**, 036601 (2011).
- [26] M. d’Aquino, *Nonlinear Magnetization Dynamics in Thin-Films and Nanoparticles, Universita degli studi di napoli, “federico II,”* 2004.
- [27] J. C. Slonczewski, “Current-driven excitation of magnetic multilayers” *J. Magn. Magn. Mater.* **159**, L1 (1996).
- [28] L. Berger, “Emission of spin waves by a magnetic multilayer traversed by a current” *Phys. Rev. B* **54**, 9353 (1996).
- [29] L. Vila, T. Kimura, and Y. Otani, “Evolution of the Spin Hall Effect in Pt Nanowires: Size and Temperature Effects” *Phys. Rev. Lett.* **99**, 226604 (2007).
- [30] a. Ganguly, K. Kondou, H. Sukegawa, S. Mitani, S. Kasai, Y. Niimi, Y. Otani, and A. Barman, “Thickness dependence of spin torque ferromagnetic resonance in Co₇₅Fe₂₅/Pt bilayer films” *Appl. Phys. Lett.* **104**, 072405 (2014).
- [31] D. C. Ralph and M. D. Stiles, “Spin transfer torques” *J. Magn. Magn. Mater.* **320**, 1190 (2008).
- [32] M. Tsoi, a. Jansen, J. Bass, W.-C. Chiang, M. Seck, V. Tsoi, and P. Wyder, “Excitation of a Magnetic Multilayer by an Electric Current” *Phys. Rev. Lett.* **80**, 4281 (1998).

- [33] H. Maehara, H. Kubota, Y. Suzuki, T. Seki, K. Nishimura, Y. Nagamine, K. Tsunekawa, A. Fukushima, H. Arai, T. Taniguchi, H. Imamura, K. Ando, and S. Yuasa, “High Q factor over 3000 due to out-of-plane precession in nano-contact spin-torque oscillator based on magnetic tunnel junctions” *Appl. Phys. Express* **7**, 023003 (2014).
- [34] H. Maehara, H. Kubota, Y. Suzuki, T. Seki, K. Nishimura, Y. Nagamine, K. Tsunekawa, A. Fukushima, A. M. Deac, K. Ando, and S. Yuasa, “Large Emission Power over 2 μ W with High Q Factor Obtained from Nanocontact Magnetic-Tunnel-Junction-Based Spin Torque Oscillator” *Appl. Phys. Express* **6**, 113005 (2013).
- [35] T. Chen, R. K. Dumas, A. Eklund, P. K. Muduli, A. Houshang, A. A. Awad, P. Dürrenfeld, B. G. Malm, A. Rusu, and J. Åkerman, “Spin-Torque and Spin-Hall Nano-Oscillators”, arXiv:1512.03162 (2015).
- [36] V. E. Demidov, S. Urazhdin, E. R. J. Edwards, M. D. Stiles, R. D. McMichael, and S. O. Demokritov, “Control of Magnetic Fluctuations by Spin Current” *Phys. Rev. Lett.* **107**, 107204 (2011).
- [37] S. E. Russek, W. H. Rippard, T. Cecil, and R. Heindl, in *Handb. Nanophysics Funct. Nanomater.* (2010), pp. 38–1.
- [38] E. Iacocca, O. Heinonen, P. K. Muduli, and J. Åkerman, “Generation linewidth of mode-hopping spin torque oscillators” *Phys. Rev. B* **89**, 054402 (2014).
- [39] J. C. Sankey, I. N. Krivorotov, S. I. Kiselev, P. M. Braganca, N. C. Emley, R. A. Buhrman, and D. C. Ralph, “Mechanisms limiting the coherence time of spontaneous magnetic oscillations driven by dc spin-polarized currents” *Phys. Rev. B* **72**, 224427 (2005).
- [40] P. K. Muduli, O. G. Heinonen, and J. Åkerman, “Temperature dependence of linewidth in nanocontact based spin torque oscillators: Effect of multiple oscillatory modes” *Phys. Rev. B* **86**, 174408 (2012).

- [41] T. J. Silva and M. W. Keller, “Theory of Thermally Induced Phase Noise in Spin Torque Oscillators for a High-Symmetry Case” *IEEE Trans. Magn.* **46**, 3555 (2010).
- [42] D. V Berkov, in *Handb. Magn. Adv. Magn. Mater.* (John Wiley & Sons, Ltd, 2007).
- [43] J. Grollier, V. Cros, and A. Fert, “Synchronization of spin-transfer oscillators driven by stimulated microwave currents” *Phys. Rev. B* **73**, 060409 (2006).
- [44] S. Sani, J. Persson, S. M. Mohseni, Y. Pogoryelov, P. K. Muduli, a Eklund, G. Malm, M. Käll, a Dmitriev, and J. Åkerman, “Mutually synchronized bottom-up multi-nanocontact spin-torque oscillators.” *Nat. Commun.* **4**, 2731 (2013).
- [45] S. Kaka, M. R. Pufall, W. H. Rippard, T. J. Silva, S. E. Russek, and J. A. Katine, “Mutual phase-locking of microwave spin torque nano-oscillators” *Nature* **437**, 389 (2005).
- [46] F. B. Mancoff, N. D. Rizzo, B. N. Engel, and S. Tehrani, “Phase-locking in double-point-contact spin-transfer devices” *Nature* **437**, 393 (2005).
- [47] A. N. Slavin and V. S. Tiberkevich, “Theory of mutual phase locking of spin-torque nanosized oscillators” *Phys. Rev. B* **74**, 104401 (2006).
- [48] X. Chen and R. H. Victora, “Phase locking of spin-torque oscillators by spin-wave interactions” *Phys. Rev. B* **79**, 180402 (2009).
- [49] R. K. Dumas, E. Iacocca, S. Bonetti, S. R. Sani, S. M. Mohseni, A. Eklund, J. Persson, O. Heinonen, and J. Åkerman, “Spin-wave-mode coexistence on the nanoscale: A consequence of the oersted-field-induced asymmetric energy landscape” *Phys. Rev. Lett.* **110**, 257202 (2013).
- [50] M. Madami, E. Iacocca, S. Sani, G. Gubbiotti, S. Tacchi, R. K. Dumas, J. Åkerman, and G. Carlotti, “Propagating spin waves excited by spin-transfer torque: A combined electrical and optical study” *Phys. Rev. B* **92**, 024403 (2015).

- [51] M. A. Hoefer, T. J. Silva, and M. D. Stiles, “Model for a collimated spin-wave beam generated by a single-layer spin torque nanocontact” *Phys. Rev. B* **77**, 144401 (2008).
- [52] A. Houshang, E. Iacocca, P. Dürrenfeld, S. R. Sani, J. Åkerman, and R. K. Dumas, “Spin-wave-beam driven synchronization of nanocontact spin-torque oscillators” *Nat. Nanotechnol.* **11**, 280 (2015).
- [53] C.-F. Pai, Y. Ou, L. H. Vilela-Leão, D. C. Ralph, and R. A. Buhrman, “Dependence of the efficiency of spin Hall torque on the transparency of Pt/ferromagnetic layer interfaces” *Phys. Rev. B* **92**, 064426 (2015).
- [54] S. Sayed, V. Q. Diep, K. Y. Camsari, and S. Datta, “Spin Funneling for Enhanced Spin Injection into Ferromagnets” *Sci. Rep.* **6**, 28868 (2016).
- [55] C.-F. Pai, M.-H. Nguyen, C. Belvin, L. H. Vilela-Leão, D. C. Ralph, and R. A. Buhrman, “Enhancement of perpendicular magnetic anisotropy and transmission of spin-Hall-effect-induced spin currents by a Hf spacer layer in W/Hf/CoFeB/MgO layer structures” *Appl. Phys. Lett.* **104**, 082407 (2014).
- [56] D. H. Ngai, *Using Picosecond Heat Pulses to Measure Magnetization*, Cornell University, 2016.
- [57] J. M. Jiang, *Photoconductivity Study of Conduction Band Carrier Concentration in Sputtered ZnO Films*, Cornell University, 2015.
- [58] J. C. Sankey, P. M. Braganca, A. G. F. Garcia, I. N. Krivorotov, R. A. Buhrman, and D. C. Ralph, “Spin-Transfer-Driven Ferromagnetic Resonance of Individual Nanomagnets” *Phys. Rev. Lett.* **96**, 227601 (2006).
- [59] A. A. Tulapurkar, Y. Suzuki, A. Fukushima, H. Kubota, H. Maehara, K. Tsunekawa, D. D. Djayaprawira, N. Watanabe, and S. Yuasa, “Spin-torque diode effect in magnetic tunnel junctions” *Nature* **438**, 339 (2005).
- [60] H. Kubota, A. Fukushima, K. Yakushiji, T. Nagahama, S. Yuasa, K. Ando, H. Maehara, Y. Nagamine, K. Tsunekawa, D. D. Djayaprawira, N. Watanabe, and

- Y. Suzuki, “Quantitative measurement of voltage dependence of spin-transfer torque in MgO-based magnetic tunnel junctions” *Nat. Phys.* **4**, 37 (2008).
- [61] J. C. Sankey, Y.-T. Cui, J. Z. Sun, J. C. Slonczewski, R. A. Buhrman, and D. C. Ralph, “Measurement of the spin-transfer-torque vector in magnetic tunnel junctions” *Nat. Phys.* **4**, 67 (2008).
- [62] F. Guo, J. M. Bartell, and G. D. Fuchs, “Ferromagnetic resonance phase imaging in spin Hall multilayers” *Phys. Rev. B* **93**, 144415 (2016).
- [63] M. Harder, Z. X. Cao, Y. S. Gui, X. L. Fan, and C.-M. Hu, “Analysis of the line shape of electrically detected ferromagnetic resonance” *Phys. Rev. B* **84**, 054423 (2011).
- [64] A. M. Gonçalves, I. Barsukov, Y.-J. Chen, L. Yang, J. A. Katine, and I. N. Krivorotov, “Spin torque ferromagnetic resonance with magnetic field modulation” *Appl. Phys. Lett.* **103**, 172406 (2013).
- [65] Z. Duan, C. T. Boone, X. Cheng, I. N. Krivorotov, N. Reckers, S. Stienen, M. Farle, and J. Lindner, “Spin-wave modes in permalloy/platinum wires and tuning of the mode damping by spin Hall current” *Phys. Rev. B* **90**, 024427 (2014).
- [66] Z. Duan, I. N. Krivorotov, R. E. Arias, N. Reckers, S. Stienen, and J. Lindner, “Spin wave eigenmodes in transversely magnetized thin film ferromagnetic wires” *Phys. Rev. B* **92**, 104424 (2015).
- [67] L. Yang, R. Verba, V. Tiberkevich, T. Schneider, A. Smith, Z. Duan, B. Youngblood, K. Lenz, J. Lindner, A. N. Slavin, and I. N. Krivorotov, “Reduction of phase noise in nanowire spin orbit torque oscillators” *Sci. Rep.* **5**, 16942 (2015).